Process and materials design for laser cladded inconel-625/tungsten carbide wear-resistant composite coatings

Eyitayo Olatunde Olakanmi (olakanmie@biust.ac.bw)
Botswana International University of Science and Technology
Shaik Hoosain
Sunday Albert Lawal
Sisa Lesley Pityana

Research Article

Keywords: Wear resistance, Inconel 625/WC composite, Carbide dissolution, Co-efficient of friction (COF), Inter-metallics

Posted Date: June 27th, 2022

DOI: https://doi.org/10.21203/rs.3.rs-1749833/v1

Process and materials design for laser cladded inconel-625/tungsten carbide wear-resistant composite coatings

Eyitayo Olatunde Olakanmi*[1, 2, 3]; Shaik. Hoosain[4]; Sunday Albert Lawal[5]; Sisa Lesley Pityana[4]

[1]Department of Mechanical, Energy & Industrial Engineering, Botswana international University of Science & Technology, Palapye, Botswana.

[2]UNESCO Chair on Advanced Manufacturing (UCAM), Botswana International University of Science & Technology, Palapye, Botswana.

[3]Advanced Manufacturing & Engineering Education (AMEE) Research Group, Botswana International University of Science & Technology, Palapye, Botswana.

[4]National Laser Centre/Laser Enabled Manufacturing Research Group, Council for Scientific & Industrial Research (CSIR), Pretoria. South Africa.

[5]Department of Mechanical Engineering, Federal University of Technology, Minna, Niger State. Nigeria.

*Corresponding author: olakanmie@biust.ac.bw

Abstract

Tailoring materials' microstructural characteristics to meet mechanical functional requirements is quite critical in designing wear resistant coatings. To the best of our knowledge, no study had related carbide dissolution ratio (CDR) in laser cladded (LC) Inconel 625 coating and its microstructural parameters to its wear performance. Hence, this study explores how laser processing and materials parameters influence CDR, microhardness (MH) and volume of materials loss (VML) of fiber-laser deposited Inconel 625 composite coatings reinforced with tungsten carbide (WC-86) by employing response surface methodology (RSM) via central composite design (CCD). Furthermore, the nature of inter-relationship between the CDR in laser cladded Inconel 625 composite coatings, microstructural parameters (average mean free path and size of retained particles, and MH) as well as VML was explored to determine appropriate process and materials parameters to optimise the wear resistance of the coatings. A fully consolidated composite coating characterised with uniformly distributed retained WC-86 particle size of 40 μm; mean free path of 30μm within the Inconel 625 matrix; MH = 852 HV0.5; CDR = 77.08% has the most desirable wear resistance (VML = 9.42mm^3) when processed with appropriate laser energy density (19.70 J/mm^2), inconel content (70wt%) and shielding gas flow rates (6.00 l/min). This study provides new insight, for coating manufacturers, on how CDR and microstructural parameters can be manipulated as LC process and materials variables are altered with a view to designing most desirable wear resistant composite coating.

Key words: Wear resistance; Inconel 625/WC composite; Carbide dissolution; Co-efficient of friction (COF); Inter-metallics

1. INTRODUCTION

There is an increasing interest in materials and process design of nickel-based super-alloy composite coatings for surface modification of high value equipment in petrol-chemical and

aerospace industries. Tungsten carbide (WC) is employed as reinforcement in super-alloys composite coatings due to its high thermal conductivity, density (16.3 gcm^{-3}), hardness (1,780 $kgfmm^{-2}$), excellent retention of strength at elevated temperature of 1093^{o}C, chemical inertness and low co-efficient of thermal expansion [1-4]. Inconel 625, a variant of nickel-based super-alloys, is selected as a matrix material because it is characterised with excellent resistance to oxidation and corrosion in seawater environments, low density (8.44 gcm^{-3}) as well as high toughness [2, 5]. The wear-resistance performance of metal matrix composite (MMC) coatings has been extensively investigated [6, 7]. Yutao *et al*., [8] noted that the wear performance of MMC coatings is dependent upon (i) the degree of dissolution of reinforcing particles; (ii) the distribution of the retained WC particles within the matrix and (iii) the mean free path between the retained reinforcement particles. According to Leech *et al.* [7], and Li *et al*., [9], the interaction between these factors is such that extreme dissolution of the reinforcing particles leads to its non-uniform distribution within the matrix as well as large mean free path between the retained small-sized particles. It had been established that high wear resistant MMC samples are characterised with increasing content of retained reinforcing particles which are uniformly distributed within the matrix [7]. This could be accounted for by the reduced free mean path between the retained large-sized reinforcements which inhibits the penetration of the abrasives into the ductile matrix. On the contrary, the occurrence of high free mean path between small-sized retained reinforcements in MMCs promotes the degradation of the ductile matrix material, hence, poor wear resistance.

Furthermore, reinforcing WC particles had been introduced into ductile Inconel 625 matrix to form composite coatings by laser cladding and hybrid laser/induction heating via blending of WC powders of varying component ratios and morphologies [1, 9 - 13]. It was evident from these literature that (i) the use of WC powders having spherical morphology resulted in composite coatings characterised with lower amount of retained WC particles as they possess the tendency to dissolved more rapidly than ball-milled reinforcements; (ii) higher volume fraction of retained WC particles was established for clad prepared with powder blends having increased component ratio of WC reinforcements; and that (iii) reduced dissolution of WC particles occurred in clads upon the dissipation of lower energy density into the melt pool. Meanwhile, the degree to which tungsten carbide dissolution ratio (CDR) influences the microstructural parameters (average mean free path and size of retained particles, and MH) and volume of materials loss (VML)) of Inconel 625/WC-86 composite coatings as laser processing and material parameters (laser energy density, component ratio and shielding/carrier gas flow rates) are varied has not been established. Hence, this study employs response surface modelling (RSM) to provide new insight on the nature of relationships between laser processing and material parameters on one hand and Inconel 625 wear performance, microstructural parameters, and carbide dissolution ratio (CDR) on the other hand. Thereafter, the inter-relationship between the CDR, microstructural parameters and wear performance are established towards designing a composite coating with optimised wear resistance at appropriate carbide dissolution ratio.

2. MATERIALS AND METHOD

2.1. Experimental design and the method of analysis.

The range of varied process parameters (Table 1) employed in this study were within a limited design domain such that the stand-off distance (12mm) and overlapping ratio (50%) were kept constant [1]. Equation (1) shown below defines the energy density (ED) in J/mm^2.

$$\text{Energy density (ED)} = P/(V * d) \quad \text{(i)}$$

where P (1200 to 2000W) is the power, V (25mm/s) is the scanning velocity and d (4 mm) is the beam diameter.

The study employed central composite design (CCD) to gain insight into the influence of alteration in parameters on the coating's VML, MH, and CDR via Design Expert 7 software. 20 runs of experiments including 14 axial points and 6 central experimental points were engaged via CCD to understand how energy density (factor A), component ratio (factor B) and carrier/shielding flow rates (factor C) influence the experimental responses. The experimental responses include carbide dissolution ratio (CDR), microhardness (MH) and volume of materials loss (VML). In Table 1, each independent process variable was varied and coded to high alpha level, high level, zero level, low level and low alpha level.

Table 1: Selected process parameters used in this study [1].

Parameters	Energy density (J/mm^2)	Component ratio In:WC-86 (rev/min)	Carrier/shielding gas flow rate (l/min)
Designations	A	B	C
High alpha level (1.6818)	24.8 (2272 W)	(2.6) 96.7:3.3 (0.1)	14.72
High level (1)	21.9 (2000 W)	(2.1) 90:10 (0.5)	12.0
Zero level (0)	17.5 (1600 W)	(1.9) 80:20 (1.1)	8.0
Low level (-1)	13.1 (1200 W)	(1.6) 70:30 (1.8)	4.0
Low alpha level (-1.6818)	10.1 (928 W)	(1.5) 63.3:36.7 (2.2)	1.28
Variation range Δ_i	4.4	10.0	4.0

The data collection procedure for CDR, microstructural properties, MH and VML would be described in sections 2.2.1, 2.2.2, 2.2.3 and 2.2.4 respectively. Empirical models for analysing the nature of inter-relationship between the laser cladding process/materials parameters and VML/MH/CDR were developed via RSM second order multiple regression method presented in polynomial equation (ii):

$$y = \beta_o + \sum_{j=1}^{k} \beta_j X_j + \sum_{j=1}^{k} \beta_{jj} X_j^2 + \sum_{i<j} \sum_{j=2}^{k} \beta_{ij} X_i X_j + \varepsilon \quad \text{(ii)}$$

where y is the predicted response, β_o is a constant, β_j is the jth linear coefficient, β_{jj} is the jth quadratic coefficient, β_{ij} is the ith interaction coefficient, X_j is the independent variable, k is the number of factors and ε is the residual error. Two groups of twenty measured responses were employed in estimating the coefficients in equation (ii) via regression analysis.

2.2. Experimental procedure

Figure 1 shows the morphology of the constituent materials from which the composite coating was fabricated. Composites coatings, deposited on stainless steel AISI 304L (100 x 50 x 10 mm), were made of Inconel 625 (+45 – 90 µm) and tungsten carbide WC-86 powders (+38 – 75 µm) supplied by Kennametal SA (PTY) LTD. The composition of the powders was already presented in our earlier study [1]. Before deposition, the substrate was cleaned with acetone

with a view to removing surface impurity and consequently improve adhesion between the clad and the substrate. A 5kW IPG YLS 5000 fibre laser system, situated at the Council of scientific and industrial research (CSIR), Pretoria, South Africa, with wavelength of 1.064 µm was engaged in carrying out the laser cladding experiments. As reported in our earlier study, a 3-way coaxial nozzle system was connected to a 5-axis CNC machine and a multi-hopper powder feed system to the nozzle. Argon was used as shielding and carrier gas at varying flow rates (Table 1). A DPSF-D3 powder feed system, with an allowable particle size range of +20 to -200μm , was used for powder delivery to the melt pool. It also has three cylinders with a feed rate deviation of 2%. The powder feed rate was indirectly controlled via the rotary speed of the powder feed system. The feed rates of inconel 625 and WC-86 were determined via flowability graphs.

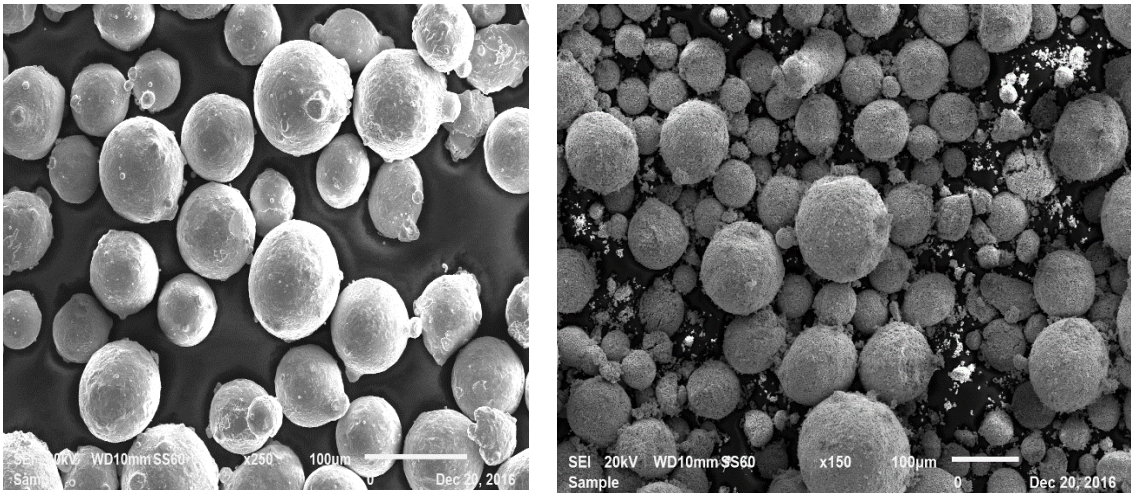

Figure 1: Scanning electron micrographs (SEM) of (a) as-received Inconel 625 and (b) as-received WC-86 powders [1]

The component ratio for each experimental condition (Table 1) was determined by considering the ratio of the feed rates of the matrix (Inconel 625) and the reinforcing particles (WC-86). Composite coating samples were fabricated in 10 tracks and four layers based on Table 2 (experimental matrix) in random order with each sample was repeated two times.

2.2.1 Macrostructural analysis

The following procedure were adopted as reported in [13] in for determining the carbide dissolution ratio (CDR):

2.2.1.1. Estimation of the amount of WC-86 captured in the melt pool (M_{WC-86}) in grams: Both Inconel 625 and composite coatings were initially deposited in ten tracks and four multilayers under the same processing conditions (Tables 1 & 2) and substrate dimensions. Deposited mass of Inconel 625 and composite coatings were designated as $M_{Inconel\,625}$ and M_{Comp} respectively.

M_{WC-86} was determined according to equation (iii) under the assumption that negligible alteration in volume of the melt pool occurred during solidification process and powder capture is not 100% efficient.

$$M_{WC-86} = M_{Comp} - M_{Inconel\,625} \quad \text{(iii)}$$

Table 2: Experimental layout for input variables and responses

Std Run	Normal Run	Factor 1	Factor 2	Factor 3	Response 1	Response 2	Response 3
		A:Energy Density (J/mm^2)	B:Inconel Content (wt%)	C:Shielding Gas Flow Rates (L/min)	Carbide Dissolution Ratio (CDR)	Microhardness (MH) (HV)	Volume of Materials Loss (VML) ($mm^{3)}$
11	1	0	-1.68179	0	72.8043	909.2	4.82
20	2	0	0	0	66.0735	713.3	99.83
10	3	1.68179	0	0	82.4076	554.5	4089.3
8	4	1	1	1	71.8632	460.84	5785.72
19	5	0	0	0	72.3873	592	904.31
14	6	0	0	1.68179	67.6659	719.7	37.74
3	7	-1	1	-1	84.9312	384.3	23179.3
18	8	0	0	0	69.2296	659.8	183.79
1	9	-1	-1	-1	58.2446	743.45	62.68
2	10	1	-1	-1	73.8971	712.2	115.99
16	11	0	0	0	61.0206	660.6	149.85
5	12	-1	-1	1	58.5004	432.3	3729.78
7	13	-1	1	1	64.5987	387.2	19329
12	14	0	1.68179	0	82.346	287.6	23792.1
17	15	0	0	0	71.5649	536.5	4082.81
6	16	1	-1	1	81.67	770.34	21.65
15	17	0	0	0	70.6924	672.3	131.21
9	18	-1.68179	0	0	66.44	237.12	24808.5
13	19	0	0	-1.68179	66.4499	674.9	153.11
4	20	1	1	-1	72.4514	399.6	14494.2

2.2.1.2 Volume fraction of WC-86 ($VF_{WC-86(C)}$) captured and retained ($VF_{WC-86(R)}$): The volume fraction of WC-86 ($VF_{WC-86(C)}$) captured in the melt pool was determined via equation (iv)

$$(VF_{WC-86(C)}) = \left({V_{WC-86(C)}} \Big/ {(V_{WC-86(C)} + V_{Inconel\ 625\ (C)})} \right) x\ 100\% \qquad \text{(iv)}$$

The volume fraction of WC-86 particles ($VF_{WC-86(C)}$) captured during LC processing is defined as ratio of the volume of the WC-86 capture to the total volume of the composite coating. The volume of WC-86 ($V_{WC-86(C)}$) captured was determined by multiplying M_{WC-86} with the density of WC-86 (ρ_{WC-86} = 16.3 × 10^{-3}g mm^{-3}) whereas the volume of Inconel 625 ($V_{Inconel\ 625\ (C)}$) coating deposited was obtained by multiplying $M_{Inconel\ 625}$ with its density

($\rho_{Inconel\,625}$ = 7.44 × 10^{-3}g mm^{-3}). Meanwhile, the volume fraction of WC-86 retained ($VF_{WC-86(R)}$) in the composite coating was determined via phase analysis of the micrographs taken by optical microscope as described in [14,15]. The phase analysis was carried out on samples cut from the middle of each deposited clad. The average of at least ten values was taken as the volume fraction of the WC-86 retained in the composite coating.

2.2.1.3 Dissolution ratio (D_{Ratio}): Equation (v) depicts that the dissolution ratio (D_{Ratio}) can be obtained by comparing the difference between the volume fractions of the WC-86 particles captured ($VF_{WC-86(C)}$) and WC-86 retained ($VF_{WC-86(R)}$) to the volume fraction of the WC-86 captured ($VF_{WC-86(C)}$).

$$(D_{Ratio}) = \left({[(VF_{WC-86(C)}) - (VF_{WC-86(R)})]} \Big/ {[VF_{WC-86(C)}]} \right) x\ 100\% \qquad \text{(v)}$$

2.2.2 Microstructural characterization

Since the deposition is continuous at the middle of the tracks, cross-sections of the deposited coating samples were obtained at the middle of the track for microstructural and compositional characterisation. The sectioned coating samples were then ground and polished to a 0.04 µm (OP-S suspension) surface finish with a Struers TegraForce-5 auto/manual polisher. Thereafter, coating samples were electro-etched in 10% Oxalic acid agent at 4.95v so that the microstructural characteristics were determined by Olympus optical microscope equipped with Analysis® software. A scanning electron microscope (SEM), Jeol JSM-7100F equipped with energy dispersive X-ray spectroscopy (EDS) was used to carry out the microstructural and elemental analysis of the composites. The SEM-EDS facility equipped with a video camera for observing the sample stage as its height is controlled used the NSS software for analysis. To identify the phases present in the coating, the samples were machined to a suitable height for the instrument and then placed on a steel PXRD sample holder, with the cladded coating facing upwards. The sample was scanned on the Panalytical Aeris XRD machine from 5 to 80 2θ at 0.02 steps and 0.09°/sec. The phases in the samples were identified by comparing the diffraction pattern with known diffraction patterns contained in the software library by using Bruker EVA software. The data was analysed using total Rietveld refinement method and Bruker TOPAS v6 software.

2.2.3 Determination of microhardness of samples

Microhardness (MH) values of the composite coatings were determined by using a Vickers hardness tester (Leitz, Germany) with a load of 0.05N and a holding time of 10.0s according to ASTM E92 standards. The experimental findings (Table 2) reported in this study were the average values of the corresponding results of the two groups of experiments which was already presented in [1].

2.2.4 Wear performance of the composite coatings

The volume of material loss (VML), which indicates the wear resistance behaviour of the composite coatings, was determined by single-trace analysis technique. According to Qu & Truhan [16], it requires the scar size measurement and a single profiling trace on the scar surface. Results obtained via this technique are in good agreement with the 3-D analysis and of much higher accuracy than mass loss and 2-D analysis techniques. VML was computed via equation (vi) where h_f (estimated by equation vii) is the wear depth, R_f is the radius of the spherical surface at both ends, W the width of the wear scar and L_S is the stroke length [16]. Figure 2 illustrates a typical wear track obtained on composite coating samples which was used in estimating V_f.

$$VML = L_S \left[\left(R_f^2 \arcsin \left({}^{W}/_{2R_f} \right) \right) - \frac{W}{2}\left(R_f - h_f\right) \right] + \left[\left(\frac{\pi}{3}\right) h_f^2 \left(3R_f - h_f\right) \right] \quad \text{(vi)}$$

$$h_f = R_f - \sqrt{\left(R_f^2 - \frac{W^2}{4}\right)} \quad \text{(vii)}$$

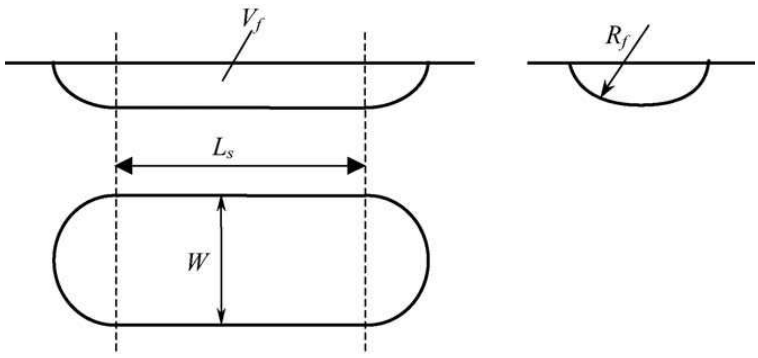

Figure 2: Wear track obtained on the flat specimen against a spherically tipped slider [16].

The following data (R_f, W and L_S) were obtained from the reciprocating–sliding friction test carried out with the R-Tec tribometer ball-on-disk tester at room temperature. The test was carried out with a 6.35 mm diameter silicon nitride (SiN_3) counter-face ball sliding against the specimen in a reciprocating motion at a constant load 100N, sliding speed (2mm/s), and at a frequency of 5Hz. Each test was replicated two times each set of conditions and the average value was taken for estimating V_f. Loading was applied on the sample vertically downwards through a motor-driven carriage that employs a load sensor in providing feedback to maintain a constant applied load.

3. RESULTS AND DISCUSSION

3.1 Development of statistical model

Mathematical models with the estimates of best fits were employed in analysing the findings from this study. The nature of the inter-relationship between the input and the output variables was elucidated by the RSM model with the analysis of variance (ANOVA) being implemented

in stepwise mode with a view to eliminating eliminate insignificant factors. To develop the mathematical models for CDR (Table 3), MH (Table 4) and VML (Table 5), ANOVA and statistics R^2, adjusted R^2, and predicted R^2 were estimated.

3.1.1 Carbide dissolution ratio (CDR) in the composite coating

The p-value < 0.05 shown in Table 3 suggests that CDR model terms are significant. This is also corroborated by the statistical model F-value of 5.60 for CDR. It is desirable that (i) the adequate precision value (9.1213) > 4 (an indication that the model can navigate the design space) and (ii) the value of lack of fit is not significant. It is evident from Table 3 that the energy density (A), the interaction between energy density an inconel content (AB), and the interaction between the inconel content and shielding gas flow rates (BC) are the factors which exercise significant influence on the CDR of the composite coatings. Comparative analysis of F-vales of factors A, AB and BC reveals the degree of the influence of the factors as follows: A $>$ AB $>$ BC. A strong correlation between the experimental and predicted values of CDR is indicated by $R^2 = 0.7655$.

Table 3: ANOVA Carbide dissolution ratio (CDR)

Source	Sum of Squares	df	Mean Square	F-value	p-value
Model	874.36	7	124.91	5.60	0.0047 significant
A-Energy Density	275.62	1	275.62	12.35	0.0043
B-Inconel Content	98.56	1	98.56	4.42	0.0574
C-Shielding Gas Flow Rates	7.26	1	7.26	0.3251	0.5791
AB	252.32	1	252.32	11.30	0.0057
AC	99.07	1	99.07	4.44	0.0569
BC	111.31	1	111.31	4.99	0.0454
A²	30.22	1	30.22	1.35	0.2672
Residual	267.86	12	22.32		
Lack of Fit	176.19	7	25.17	1.37	0.3759 not significant
Pure Error	91.67	5	18.33		
Cor Total	1142.22	19			
Std. Dev.	4.72		**R²**	0.7655	
Mean	70.81		**Adjusted R²**	0.6287	
C.V. %	6.67		**Predicted R²**	0.4820	
PRESS	591.70		**Adeq Precision**	9.1213	

The existence of a reasonable agreement between the predicted R^2 of 0.4820 and the adjusted R^2 of 0.6287 could be inferred from the difference between the values which is less than 0.2. Equation viii expressed in term of coded factors describes the quadratic relationship for estimating the CDR values of the composite coatings. The standard deviation being $\pm 6.67\%$ of the mean value of the CDR (Table 3):

CD = 69.8266 + 4.49241 * A + 2.68644 * B - 0.728997 * C - 5.61606 * AB + 3.51909 * AC - 3.73008 * BC + 1.43504 * A^2 (viii)

3.1.2 Microhardness of composite coatings

The analysis of variance for microhardness as in Table 4 shows the contribution of each input parameter as: Energy Density (A) = 0.0059, Inconel Content (B) = < 0.0001, Shielding Gas Flow Rate (C) = 0.6979. It can be deduced from the Table 4 that the model *F*-value of 17.35 implies the model is significant and the only significant model factors for the coating's microhardness (MH) are energy density (A), inconel content (B) and A^2. However, Inconel content has the most significant influence on microhardness with an F-value of 52.28. But the extent of the effects of energy density (A) and A^2 on the microhardness are significantly lower when compared to the inconel content. R^2 value of 0.8611 suggests strong correlation between the predicted and experimental data obtained for microhardness of the coatings. The value obtained for the predicted R^2 of 0.6726 is in reasonable agreement with the adjusted R^2 of 0.8115 (i.e. the difference is less than 0.2). Adequate precision measures the signal to noise ratio. Meanwhile, Sun & Hao (2012) recommended that a ratio greater than 4 is desirable, hence, the ratios of 14.7689 obtained in this study indicates an adequate signal.

Table 4: ANOVA Microhardness

Source	Sum of Squares	df	Mean Square	F-value	p-value
Model	5.217E+05	5	1.043E+05	17.35	< 0.0001 significant
A-Energy Density	63262.40	1	63262.40	10.52	0.0059
B-Inconel Content	3.143E+05	1	3.143E+05	52.28	< 0.0001
C-Shielding Gas Flow Rates	943.71	1	943.71	0.1570	0.6979
AC	22858.43	1	22858.43	3.80	0.0715
A²	1.203E+05	1	1.203E+05	20.01	0.0005
Residual	84163.92	14	6011.71		
Lack of Fit	63920.13	9	7102.24	1.75	0.2779 not significant
Pure Error	20243.79	5	4048.76		
Cor Total	6.058E+05	19			
Std. Dev.	77.54		**R²**		0.8611
Mean	575.39		**Adjusted R²**		0.8115
C.V. %	13.48		**Predicted R²**		0.6726
PRESS	1.984E+05		**Adeq Precision**		14.7689

The non-significant value obtained for lack of fit as seen in Table 4 is preferred. Analysis of finding from this study implies that the developed model is suitable for navigating the design space. Therefore, the obtained empirical relationship between the microhardness and the process parameters in terms of coded factors, having eliminated the non-significant terms, is described as follows by equation (ix) for fiber laser fabricated composite coatings with the standard deviation being ±13.4% the mean value of microhardness (Table 4):

MH = 637.216 + 68.0609 * A - 151.701 * B - 8.31273 * C + 53.4538 * AC - 90.5457 * A^2 (ix)

3.1.3 Volume of material loss (*VML*) for composite coating

Table 5 highlights the ANOVA analysis of the volume of material loss (VML) of the coatings as well as the significant model terms determined via the stepwise regression method which

eliminates the insignificant terms automatically. Again, high F-value (35.93) obtained for the model suggests that it is significant. Adequate precision (16.7221), being greater than 4, satisfies the adequate model discrimination. It is preferred that the value (2.86) of lack of fit is not significant as seen in Table 5. Furthermore, the value (0.9700) obtained for R^2 is very close to 1, an indication that the mathematical models developed for VML correlates very strongly with the experimental data. Meanwhile, energy density (A), inconel content (B) and second order of energy density (A^2) and inconel content (B^2) are the only significant factors that affect the VML of coatings as revealed by Table 5. The ultimate empirical model relating to VML, in terms of coded factors is described as follows for the coatings with the standard deviation being $\pm$35.02% of the mean value of VML (Table 5):

VML = 956.072 - 4446.75 * A + 7239.11 * B - 672.197 * C - 2321.7 * AB - 1077.45 * AC - 2016.45 * BC + 4580.2 * A^2 + 3678.49 * B^2 - 494.514 * C^2 (x)

Table 5: ANOVA for volume of material loss (VML) for composite coating

Source	Sum of Squares	df	Mean Square	F-value	p-value
Model	1.553E+09	9	1.726E+08	35.93	< 0.0001 significant
A-Energy Density	2.700E+08	1	2.700E+08	56.23	< 0.0001
B-Inconel Content	7.157E+08	1	7.157E+08	149.03	< 0.0001
C-Shielding Gas Flow Rates	6.171E+06	1	6.171E+06	1.28	0.2834
AB	4.312E+07	1	4.312E+07	8.98	0.0134
AC	9.287E+06	1	9.287E+06	1.93	0.1945
BC	3.253E+07	1	3.253E+07	6.77	0.0264
A^2	3.023E+08	1	3.023E+08	62.95	< 0.0001
B^2	1.950E+08	1	1.950E+08	40.61	< 0.0001
C^2	3.524E+06	1	3.524E+06	0.7338	0.4117
Residual	4.802E+07	10	4.802E+06		
Lack of Fit	3.559E+07	5	7.118E+06	2.86	0.1366 not significant
Pure Error	1.243E+07	5	2.487E+06		
Cor Total	1.601E+09	19			
Std. Dev.	2191.43		**R^2**	0.9700	
Mean	6257.78		**Adjusted R^2**	0.9430	
C.V. %	35.02		**Predicted R^2**	0.8199	
PRESS	2.884E+08		**Adeq Precision**	16.7221	

3.2 Confirmation of the statistical models

Equations viii, ix, and x are the predictive models for CDR, MH and VML which are represented in Figures 3, 4, and 5 respectively. All the predictive models agree very well with the experimental data for the coatings (Figures 3, 4 & 5). Adequacy of the models was validated via confirmatory tests implemented by using newly selected independent variables within the experimental range (Table 1) for each output variable. Predicted responses for CDR, MH and VML were determined via regression equations viii to x. Newly selected input factors, the measured/predicted outcomes, and the percentages of error for experimental outcomes are presented in Table 6. Except for equation x when energy density, inconel content and shielding gas flow rate are set at 19.7J/mm^2, 70wt% and 6.0 l/min (first data set) respectively, all the predictive models agree very well with the experimental data for the clads (Table 6). Further

analyses are needed to explain the non-agreement of the experimental and predicted VML values at the first data set. Meanwhile, predicted value of the VML at the first data set suggests that the silicon nitride (SiN_3) counter-face ball was wearing rather than the composite coating. Lowest value of VML (9.42 mm^3) at the first data set (Table 6) attests to the desirable wear resistant behaviour of the composite coating. The error margins for CDR, MH and VML are +10%, 6% and -4% respectively and the adequacy of the developed models is verified provided the exceptional value of V_f in equation x, for first data set, is neglected.

Table 6: Confirmatory experiments for the statistical models.

Expt. No.	**Energy density (ED)**	**Inconel content (In)**	**Gas flow (G)**		**CDR (%)**	**MH**	***VML***
1	19.7	70.0	6.0	Measured	77.08	852.59	9.42
	(0.5)	(-1)	(0.5)	Predicted	74.93	809.52	-2242.89
				Error (%)	2.87	5.40	-1004.20
2	15.3	80.0	6.0	Measured	68.43	588.56	4082.70
	(-0.5)	(0)	(0.5)	Predicted	66.69	563.03	4134.13
				Error (%)	2.61	4.53	-1.24
3	21.9	90	8.0	Measured	79.63	455.97	9320.21
	(1)	(1)	(0)	Predicted	72.82	463.03	9685.42
				Error (%)	9.35	-1.52	-3.77

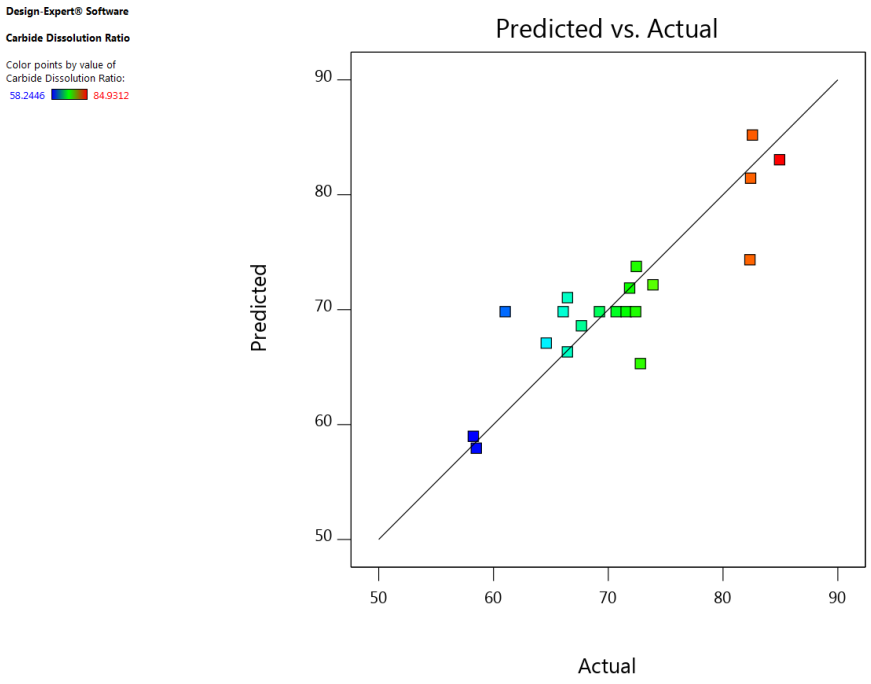

Figure 3: Predicted versus measured values of carbide dissolution ratio (CDR) for the composite coating.

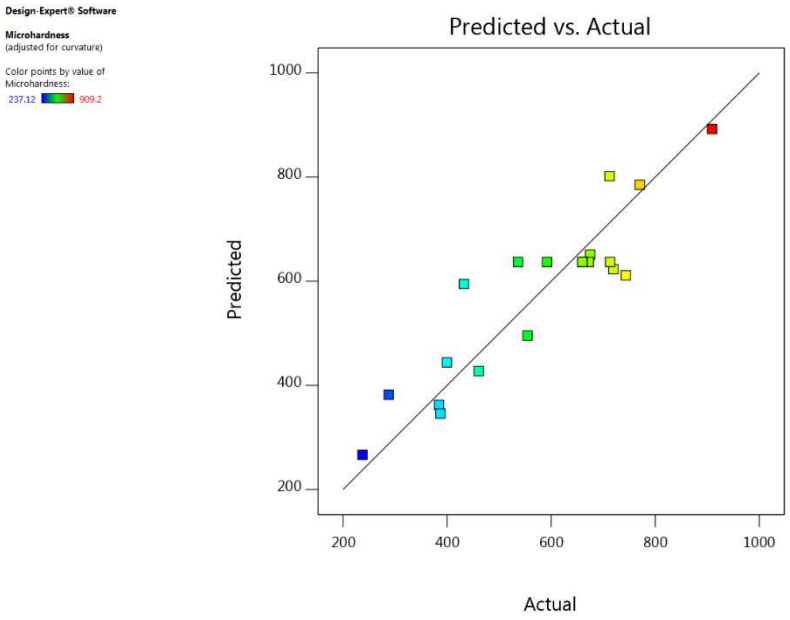

Figure 4: Predicted versus measured values of microhardness (MH) for the composite coating.

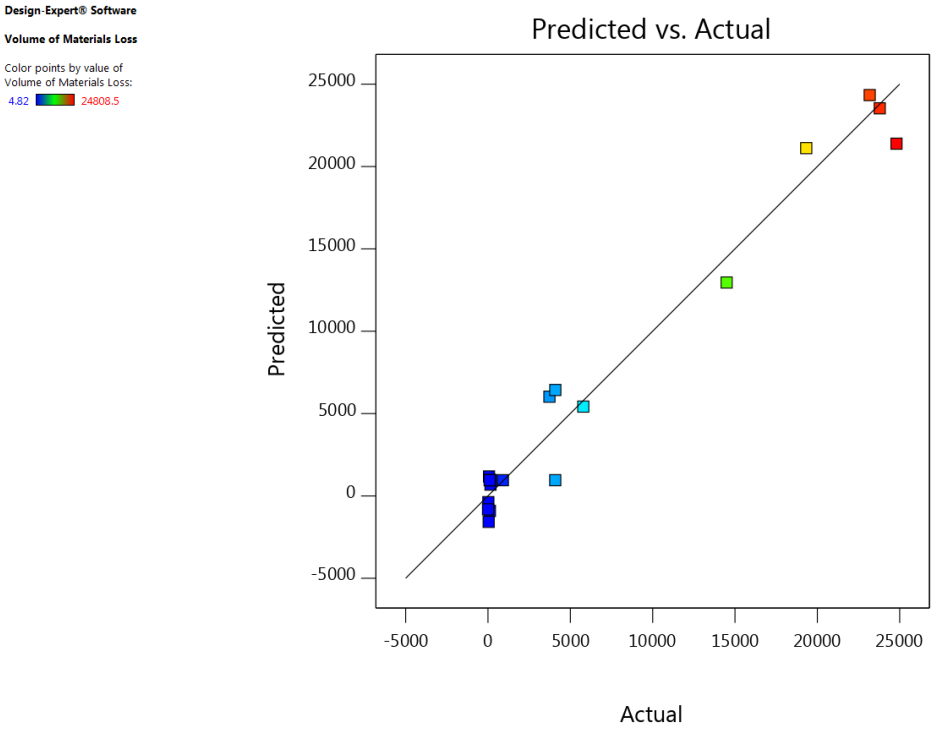

Figure 5: Predicted versus measured values of volume of materials loss (VML) for the composite coating.

3.3 Effects of process parameters on the carbide dissolution ratio (CDR) and wear performance of the composite coatings

3.3.1 Effects of process parameters on the carbide dissolution ratio of the composite coating

The influence of laser energy density (A), inconel content (B) and shielding/carrier gas flow rates (C) on the carbide dissolution ratio (CDR) is analysed via perturbation plots (Figure 6) wherein the center-point in the design space is considered. As noted earlier on, CDR is the ratio of the volume fraction of WC-86 particles dissolved to volume fraction of WC-86 particles captured. The volume fraction of WC-86 dissolved is the difference between the volume fractions of WC-86 captured and retained in the composite coatings. It is evident from Figure 6 that CDR increases as both laser energy density (A) and inconel content (B) increase. Figure 6 also reveals that the perturbation plot for laser energy density is steeper than that of inconel content, an indication that laser energy density significantly influences CDR much more than inconel content. This lends credence to the ANOVA analysis (Table 3) in which p-value for laser energy density ($p = 0.0043$) and is less than that of inconel content ($p = 0.0574$). Meanwhile, there exists a marginal inverse variation between the shielding gas flow rates and CDR. Evidence of increased dissolution of the reinforcing WC-86 particles in the melt pool as laser energy density increases (Figure 6) is also supported by Figures 7a & b in which it is seen that the size and the number of the retained WC-86 particles decrease as laser energy density increases. Furthermore, the mass of the WC-86 particles captured in the composite coating increases from 13.62g to 19.62g when laser energy density dissipated into the melt pool varied from 13.1 J/mm^2 to 21.9 J/mm^2 as inconel content and gas flow rates were held constant at 70 wt% and 12 l/min respectively.

The dissolution of WC-86 particles in inconel 625 matrix results in the formation of secondary phases or intermetallics (see region labelled A in Figures 8a to e). EDS analysis (Table 7) of the micrographs of the samples presented in Figure 8 attest to this claim on the formation of secondary phases or intermetallics as a result of inter-mixing of the constituent elements. Figures 8a & b reveal that these secondary phases are distributed in the inconel matrix as light contrast angular phases. A physical examination of the density of the light contrast angular phases within the microstructure (Figures 8a & b) was engaged in estimating the degree of WC-86 dissolution. It is evident that a higher number density of secondary phases is present in the composite sample fabricated with 21.9 J/mm^2 (Figure 8b) relative that of 13.1 J/mm^2 (Figure 8a). This outcome further confirms the previous findings which indicate that CDR increases as laser energy density increases. Increased CDR is ascribed to increase in (i) the maximum temperature encountered in the melt pool and (ii) the degree of mixing of the reinforcing particles and the Inconel 625 matrix and cooling rates as laser energy density increases. Consequently, these factors are responsible for (i) the WC-86 particles encountering increased intense heating which results in increased melting of WC-86 particles and (ii) the melt pool remaining molten much longer such that more WC-86 particles dissolve as cooling rates increases [13, 17].

Microstructural evidence obtained from Figures 7b & c also reveal that the size and number of retained WC-86 particles reduce as inconel content increases thereby lending credence to earlier finding from Figure 6. Analysis of Figures 8b & c also confirm that a higher density of

secondary phases is present in the composite sample fabricated with 90wt% In (Figure 8c) relative to that of 70wt% (Figure 8b). Increased CDR as inconel content increases could be attributed to the fact that the propensity for full melting and effective inter-mixing of WC-86 particles within the matrix increases because the available energy density is sufficient to melt a blend containing higher proportion of lower melting point Inconel 625 matrix (1350^{o}C) and fewer proportion higher melting point WC-86 particles (2870^{o}C). Hence, the occurrence of full melting (an indication of higher CDR) as evident in Figures 8b & c as inconel content increases.

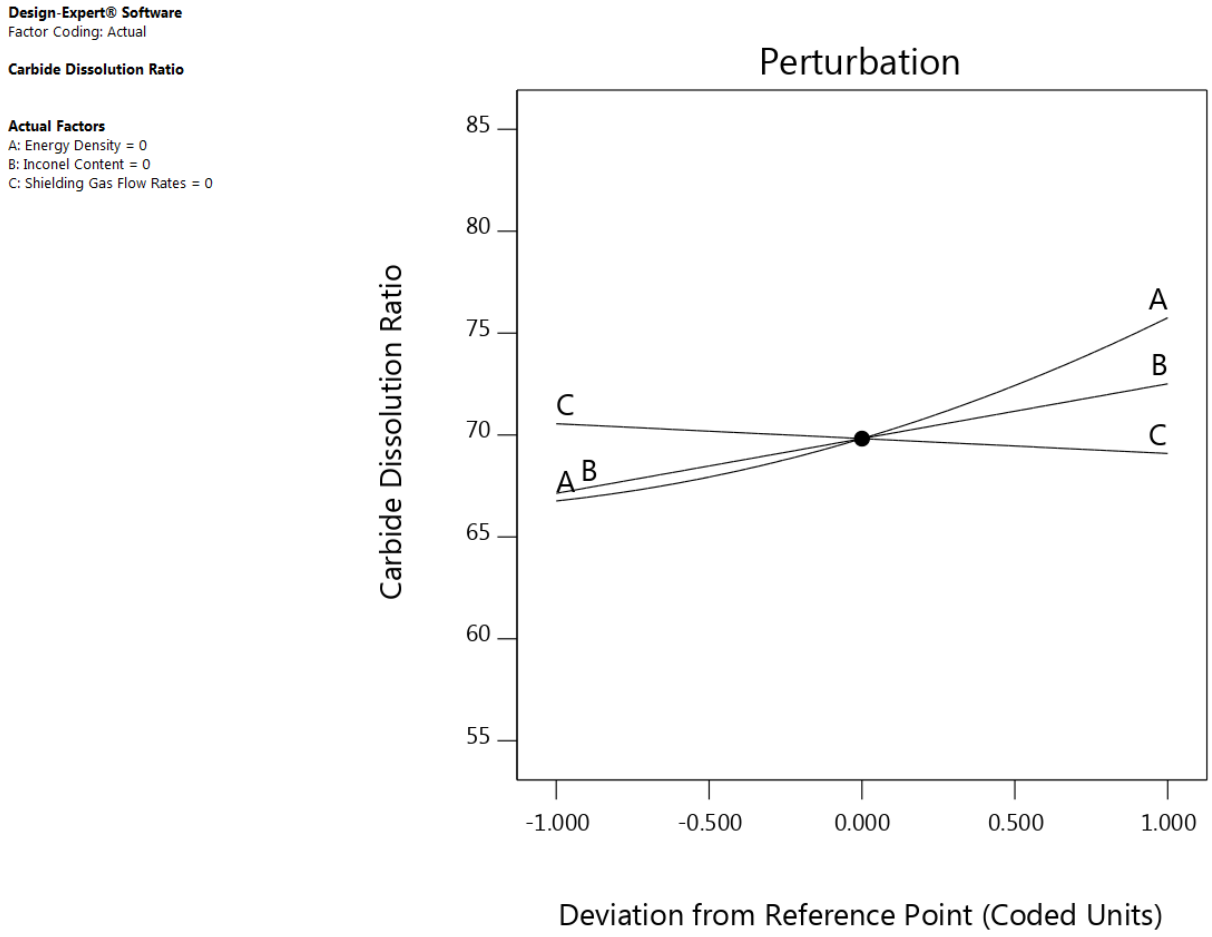

Figure 6: Effects of all factors on the carbide dissolution ratio (CDR) of composite coatings.

Meanwhile, reduced CDR reported at lower Inconel 625 matrix content when the proportion of higher melting point WC-86 in the blend is increasing is accounted for by partial dissolution of reinforcing particles (Figure 7b) in the melt pool as the available laser energy density is insufficient to melt the powder blends (especially the higher melting point WC-86 particles portion) fully. Reduced number density of secondary phases noticed in Figure 8b also attests to these findings. Reduced CDR reported when the flow rate of shielding gas increases could be ascribed to its increased cooling effect which reduced the intensity of the laser energy density required to dissolve the reinforcing WC-86 particles introduced into the melt pool. Increased CDR noted at lower flow rates of shielding gas is due to its declining capability to cool down the molten pool.

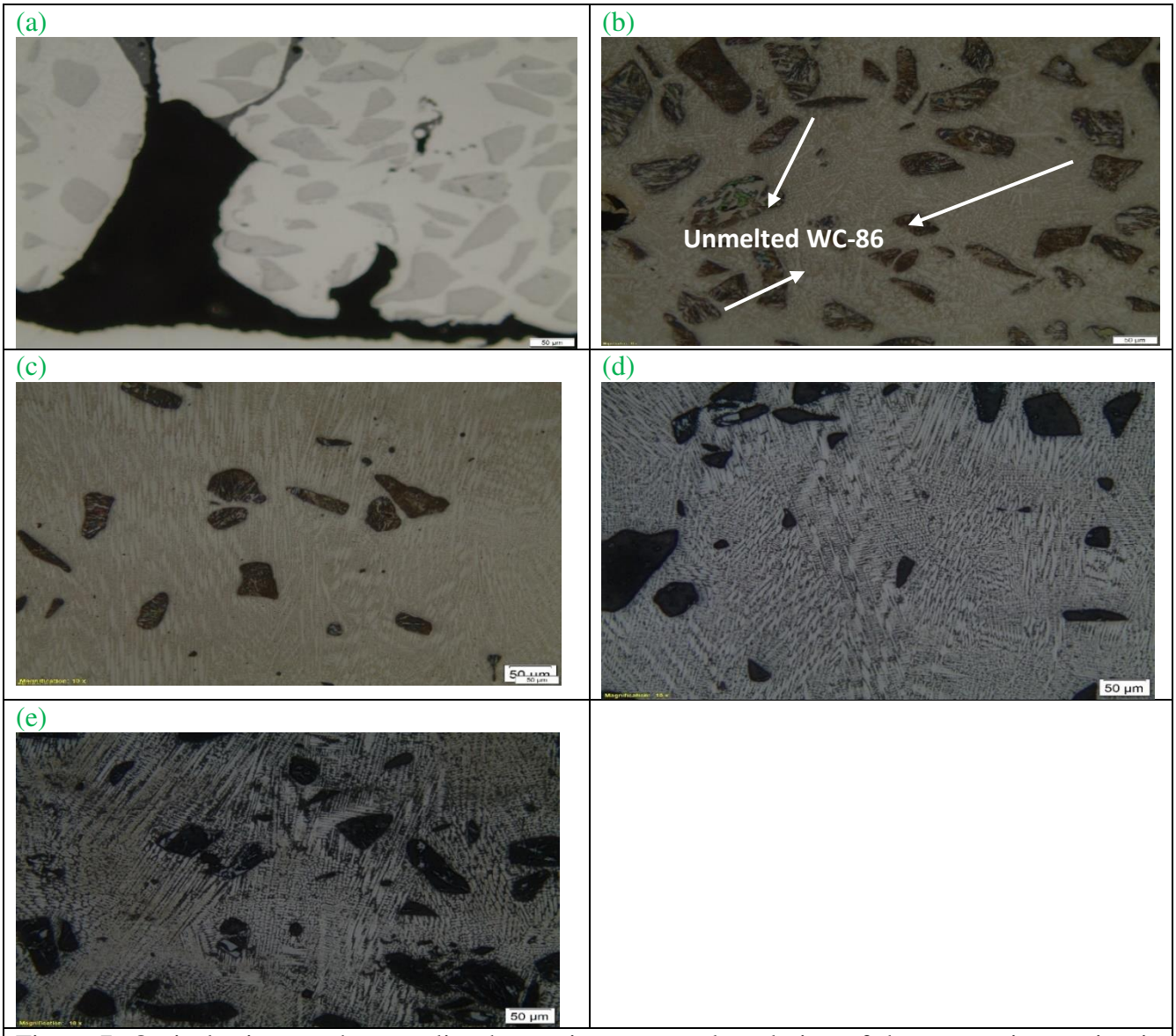

Figure 7: Optical micrographs revealing how microstructural evolution of the composite coating is influenced by alteration in process and materials parameters (a) 13.1 J/mm^2, 70wt% In, 12l/min; (b) 21.9 J/mm^2 70wt% In, 12l/min; (c) 21.9 J/mm^2, 90wt% In, 12l/min; (d) 13.1 J/mm^2, 90wt% In, 4l/min; (e) 13.1 J/mm^2, 90wt% In, 12l/min.

Table 7: EDS of different of micrographs of cladded composite coatings (see region labelled A in Figures 8a to e) fabricated with various laser process and material parameters

Samples	***C***	***O***	***Al***	***Si***	Ti	Cr	Mn	Fe	Co	Ni	Nb	Mo	W
a	1.00	25.47	4.51	2.90	1.30	29.23	2.04	2.00	3.95	45.10	25.99	1.44	2.30
b	0.93	26.16	2.60	2.89	1.30	30.79	4.94	5.37	18.17	23.00	12.66	1.33	12.60
c	0.80	25.89	2.55	4.24	0.60	35.10	2.25	6.70		51.80	22.76	1.43	0.68
d	0.70	24.92	1.57	0.51		44.01	0.47	3.00		64.20	20.13	1.11	0.67
e	0.95	25.17	4.28	1.96	0.70	37.09	2.24	2.60	2.50	59.20	21.63	1.01	0.64

Therefore, the attainable maximum temperature of the molten pool at lower flow rates of the shielding gas is higher than at higher flow rates, hence, increased CDR reported at lower flow

rates. Analysis of Figures 7d and e as well as Figures 8d and e confirms the claim that CDR decreases with increasing shielding gas flow rates (Figure 6). For instance, it is evident from Figures 7d & e that the size and number of retained WC-86 particles is noticeably increasing slightly as shielding gas flow rates increases from 4l/min to 12l/min. In consensus with Figure 6, analysis of Figures 8d & e also confirms that there exists a marginal increase in density of secondary phases in the composite sample fabricated with 4l/min (Figure 8d) in comparison to that of 12l/min (Figure 8e). Future studies will employ XRD to explore the nature of phases present in the composite coatings and how the phase composition in the cladded composite coatings influence its wear resistance behaviour.

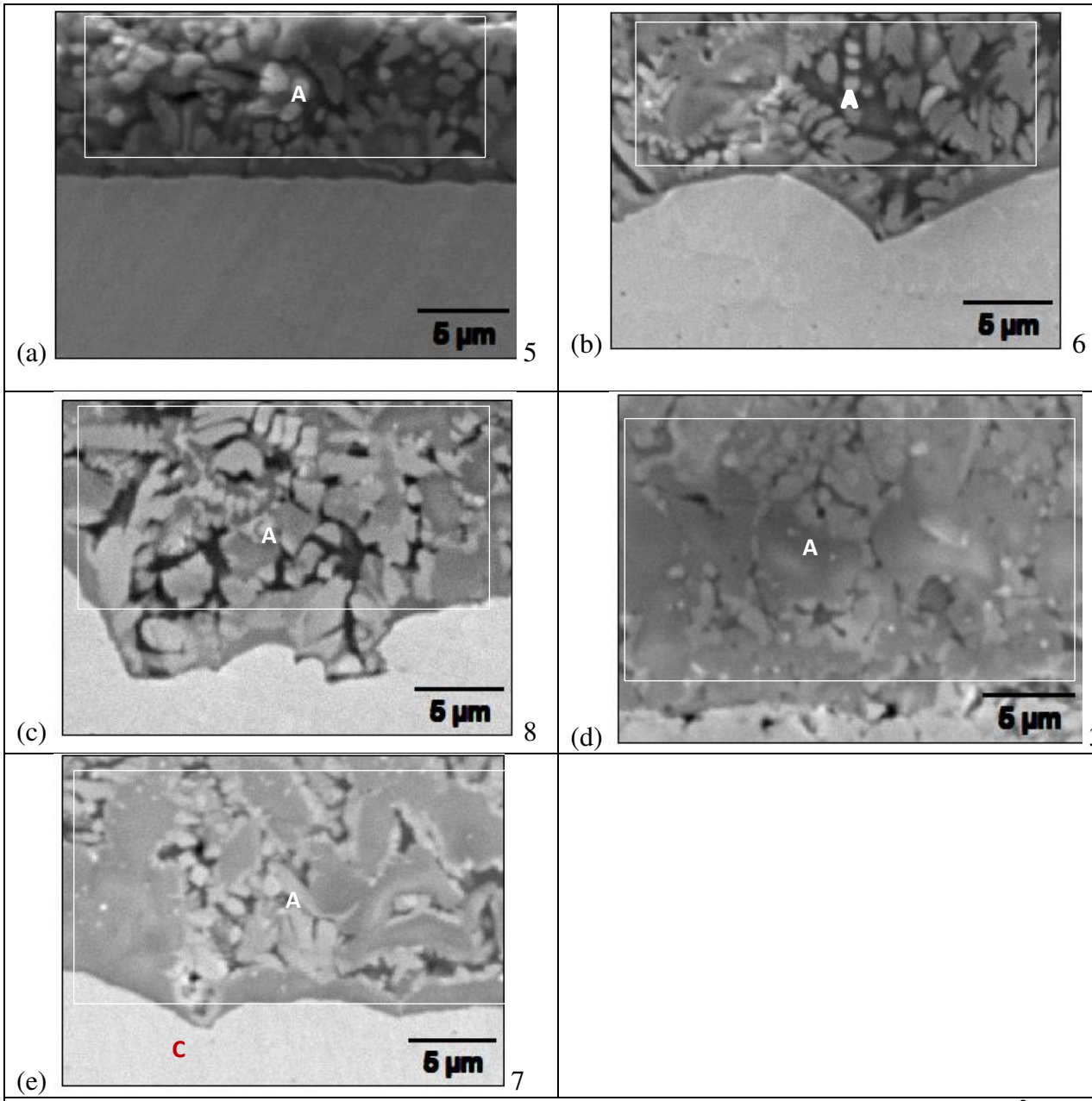

Figure 8: SEM/BSE images of the cross-sectioned clad layer formed at (a) 13.1 J/mm^2, 70wt% In, 12l/min; (b) 21.9 J/mm^2 70wt% In, 12l/min; (c) 21.9 J/mm^2, 90wt% In, 12l/min; (d) 13.1 J/mm^2, 90wt% In, 4l/min; (e) 13.1 J/mm^2, 90wt% In, 12l/min, showing the dissolution around the retained WC-86 boundary.

It is evident from Figure 9a that the lowest CDR (< 50%) is obtainable when process parameter was set at lowest values of laser energy density (13.1 J/mm^2) and inconel content (70 wt%). This outcome is consequent upon insufficient laser energy density being employed to process a powder blend consisting of highest proportion of higher melting point WC-86 particles. Hence, the resultant coating sample contains a pre-ponderance of partially melted WC-86 particles (Figure 7a). Highest value of CDR (78%) is obtained when highest energy density (21.9 J/mm^2) is combined with lowest Inconel content (70 wt%) to process the composite coating. A combination of highest laser energy density (21.9 J/mm^2) with highest Inconel content (90wt%) results in reduction of CDR (72.5%) whereas employment of lowest energy density (13.1 J/mm^2) alongside highest inconel content (90wt%) results in 75% CDR. Figure 9b shows that highest CDR (78%) is attainable by combining highest laser energy density (21.9 J/mm^2) with highest flow rates of shielding gas (12l/min) whereas lowest CDR (62%) is achievable by combining lowest energy density (13.1 J/mm^2) with highest shielding gas flow rates (12l/min). Meanwhile, CDR is seen to vary between 66% to 72% as shielding gas is held constant at lowest level and laser energy density is altered between lowest to highest level. Figure 9c indicates that lowest CDR (55%) is achievable by setting process parameter at lowest values of shielding gas flow rates (4l/min) and inconel content (70wt%) while highest CDR (76%) was obtained by combining highest inconel content (90wt%) with lowest shielding gas flow rates (4l/min). By keeping the shielding gas flow rates at the highest level (12l/min), the CDR is seen to vary between 68% to 79% as Inconel content is altered from the lowest to highest level. Finally, comparative analysis of the range of CDR values obtainable for the influence of the parameters interactions indicates that laser energy/Inconel content (CDR =30%) > Inconel/shielding gas flow rates (CDR = 20%) > shielding gas flow rates/laser energy density (CDR = 16%). This conforms to F-values of the interactions of factors AB, BC and AC.

3.3.2 Effects of process parameters on the microhardness of the laser cladded composite coating.

Figure 10 highlights the influence of energy density (A), inconel content (B) and gas flow rates (C)) on the coating's microhardness. As the laser energy density increases, the coating's microhardness increases to the maximum upon setting the laser energy density at 19.7 J/mm^2, whereas. the microhardness of the coatings decreases as laser energy density is increased above 19.7 J/mm^2. In concurrence with Zeng *et al.,* [19] who varied energy density by changing scanning speed while holding constant (laser power and beam diameter), alteration in the applied laser energy density induces varying degree of dissolution of the reinforcements in the melt pool which consequently impart varying functional performance such as microhardness (Figures 6, 7 and 10). Observation of micrographs (Figure 7) of samples fabricated with 70wt% In and 12l/min as laser energy density varies between 13.1 J/mm^2 to 21.9 J/mm^2 affirm this claim.

Figure 7a shows the micrograph, of the composite coating deposited with 13.1 J/mm^2, which is characterised with porosities cracks, and poor bonding between the reinforcement and the inconel 625 matrix. It is evident from Figure 7a that laser energy density of 13.1 J/mm^2 is incapable of consolidating the powder blends effectively, hence, the poor densification of the coating characterised with very low microhardness (432.3 $HV_{0.5}$). However, the dissipation of 21.9 J/mm^2 into the molten pool induces a densely and uniformly distributed WC-86 particles within the Inconel 625 matrix (Figure 7b), hence a relatively higher microhardness (770.34 $HV_{0.5}$) it exhibits as seen in Figure 10 and Table 2. Analysis of Figure 10 shows that the

microhardness imparted to the coating at laser energy density of 21.9 J/mm^2 was less than that at 19.7 J/mm^2.

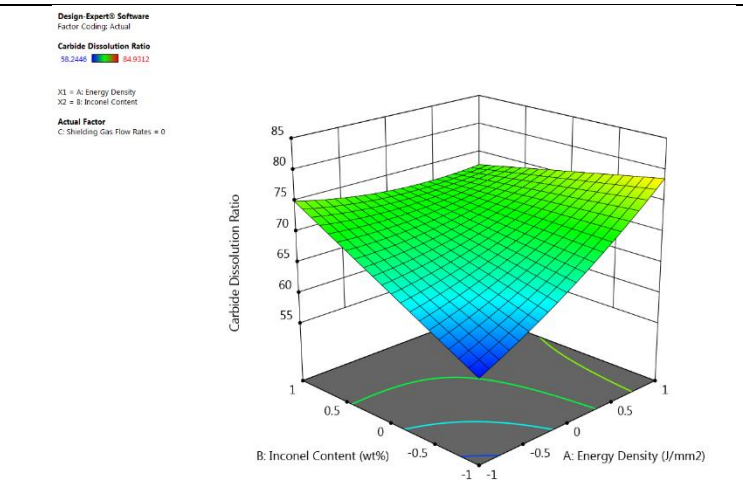

(a)

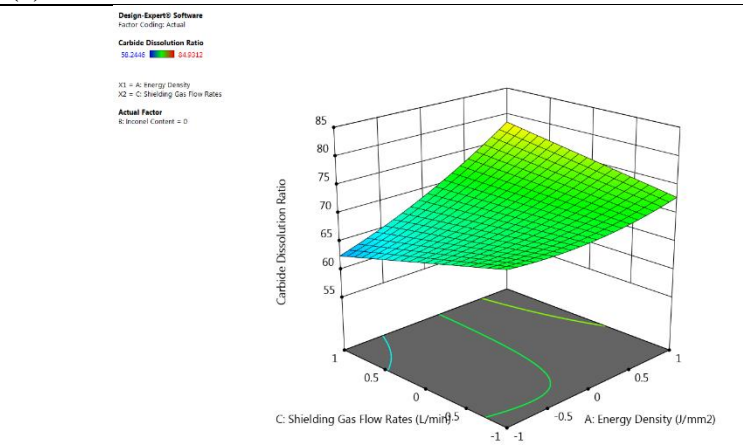

(b)

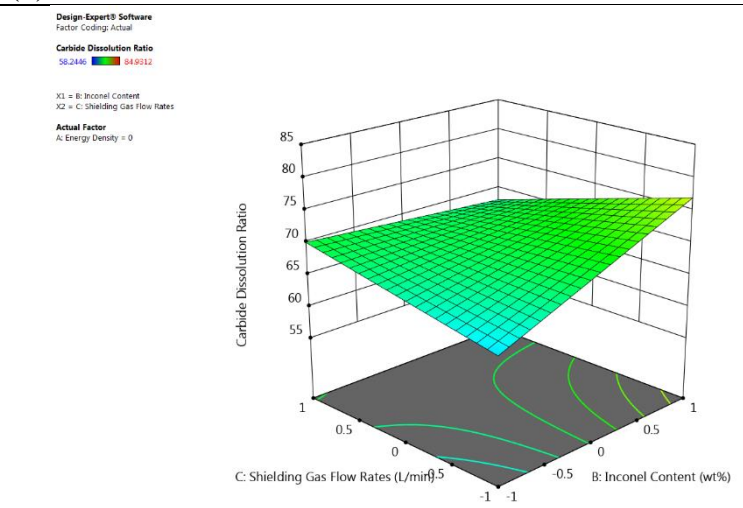

(c)

Figure 9: 3-D plots showing the effects of (a) Energy density versus Inconel content, (b) Energy density versus Gas flow rates and (c) Inconel content versus Gas flow rates on the carbide dissolution ratio (CDR) of the composite coating.

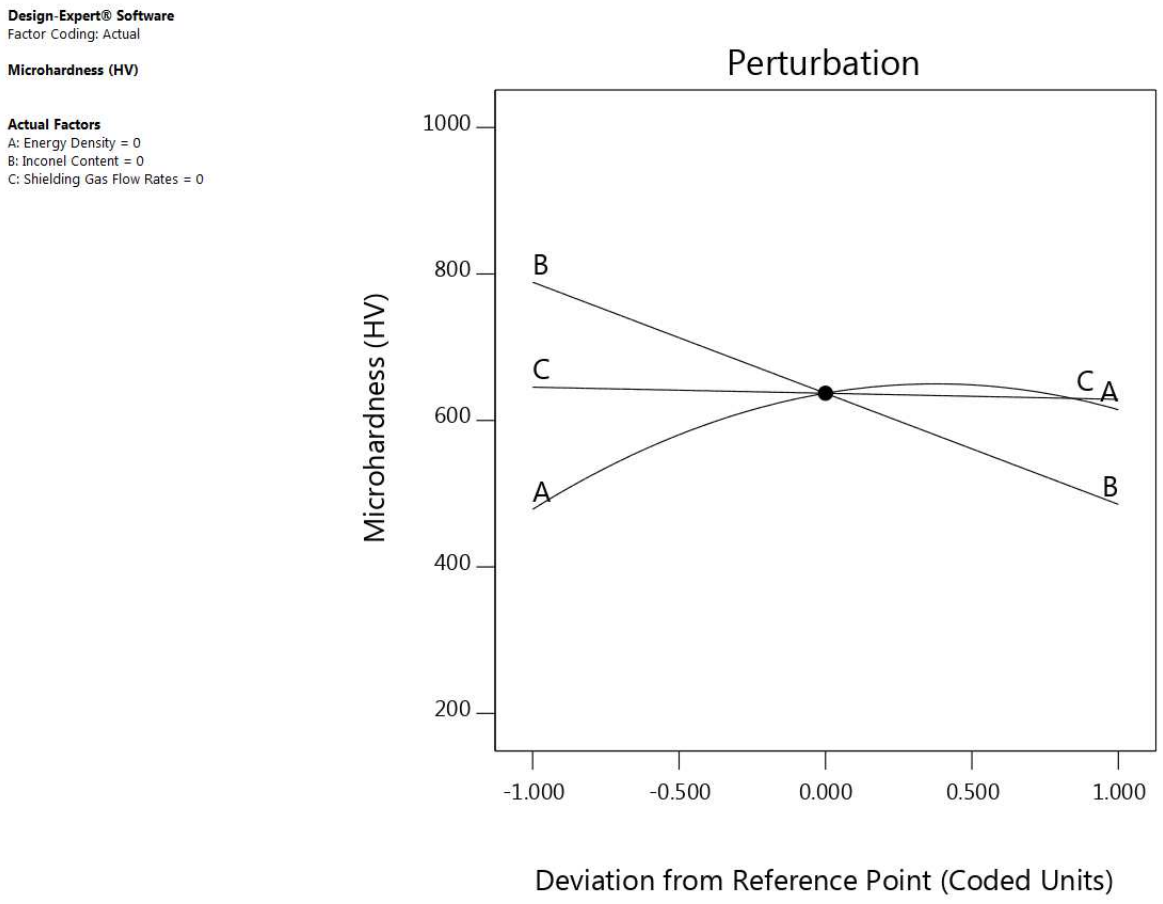

Figure 10: Effects of all factors on the microhardness (MH) of the composite coatings [1].

Comparative analysis of Figures 6 and 10 reveals that coating's microhardness was optimised at laser energy density of 19.7 J/mm^2 when CDR ~ 72.50%. The lower microhardness reported for laser energy density above 19.7 J/mm^2 could however be attributed to the WC-86 particles dissolving excessively and reacting with the constituents of the Inconel 625 to form intermetallic compounds characterised with lower hardness values than those of WC-86 particles and optimised composite coating [20, 21]. There exists an indirect relationship between inconel 625 content and the coating's microhardness (Figure 10). The consolidation mechanism in this study entails incomplete metallurgical melting in which the higher melting-point reinforcement (WC-86) dissolves while the ductile Inconel 625 matrix is fully melted [19, 22]. By introducing 90wt% Inconel 625/10wt% WC-86 into the melt pool, there occurred an increment in viscosity of the composite melt because the reinforcing component of the powdered blends was full melted due to its (i) smaller proportion and (ii) high surface area to volume ratio. It is believed that increased viscosity hindered efficient flow of the melt pool since it is characterised with decreased rheology. According to Al-Hamdani *et al.,* [22] and Xu et al., [23], an intensive Marangoni convection developed within the composite melt which introduced an additional force into the pool. The melt containing 90wt% Inconel 625 eventually flows radially inward towards the laser beam center instead of spreading outward on the underlying surface because of combined influence of (i) reduced rheological characteristics of the melt due to its increased viscosity and (ii) the effect of Marangoni force. This resulted in poor consolidation mechanism due to longer solidification time of the composite melt pool. The poor consolidation mechanism accounts for microstructural defects such as porosities which reduced the microhardness of the composite coatings (Figure 7c). With the Inconel 625

content being reduced to 70wt%, the microhardness of the composite coating increases (Table 2). This is because of reduced melt pool due to partial dissolution of the reinforcements instead of encountering full melting. Consequently, melt pool was not superheated due to partial dissolution of the reinforcing particles. Hence, no occurrence of excessive in-situ chemical reactivity of the constituents of the composite blend such that no additional thermal energy was introduced into the melt pool during laser-material interaction. Therefore, the rheology of the melt was not handicapped due to reduced melt viscosity and the action of Marangoni force. In this context, the melt pool solidified within the adequate time required for the formation of pore-free microstructure and eventually resulted in increased microhardness of the coatings (Figure 7b).

Analysis of Figure 10 and Table 2 reveals that coating's microhardness is constant as the flow rates of shielding gas was altered, thereby, indicating that shielding gas flow rate has no effect on microhardness [23]. An observation of Figures 7d and e lends credence to this finding as no significant variation in the amount of dissolved reinforcing particle, porosities, and cracks are evident in the microstructure. Table 4 reveals that the interactions between the model terms are quite significant given that they influence the microhardness of the coatings. Figure 11a shows that the interactions the between inconel content and energy density. With shielding gas flow rate set at zero level, Figure 11a shows that at inconel content above 85wt% the microhardness of the composite coatings would be less than 400 HV when laser energy density less than 15.3 J/mm^2 is engaged for fabricating the claddings. When Inconel content was set between 75wt% to 85wt%, the microhardness of the coatings is seen to vary between 500 to 800 HV irrespective of the amount of energy density employed during processing. It is discernible from Figure 11a that the range of microhardness is $\sim$ 500HV.

3.3.3 Effects of process parameters on the volume of material loss (VML) of the composite coating.

The role of laser energy density, inconel content, and shielding gas flow rates in the volume of materials loss (VML) in the Inconel 625/WC-86 composite coatings and its wear mechanism are presented in Figures 12 and 13 respectively. Furthermore, Figures 12 and 13 are also elucidated in terms of the composite's microstructural features (Figure 7). Analysis of Figure 12 reveals that VML decreases as laser energy density increases 13.1 to 19.7 J/mm^2 and thereafter begins to increase as laser energy density is raised above 19.7 J/mm^2. This implies that the wear resistance of the composite is optimised by adopting an energy density of 19.7 J/mm^2 as evident by attainment of minimum VML. Furthermore, the wear resistance of composite coating is seen to deteriorate as the inconel 625 content increases. This is indicated by the increase in VML with the corresponding increase in inconel content. Figure 12 shows that the shielding gas flow rate varying between 4l/min to 8l/min has no influence on the VML of the composite coating. Meanwhile, shielding gas flow rate set above 8l/min tend to reduce VML slightly, hence, it favours improvement in wear resistance of the composite coatings.

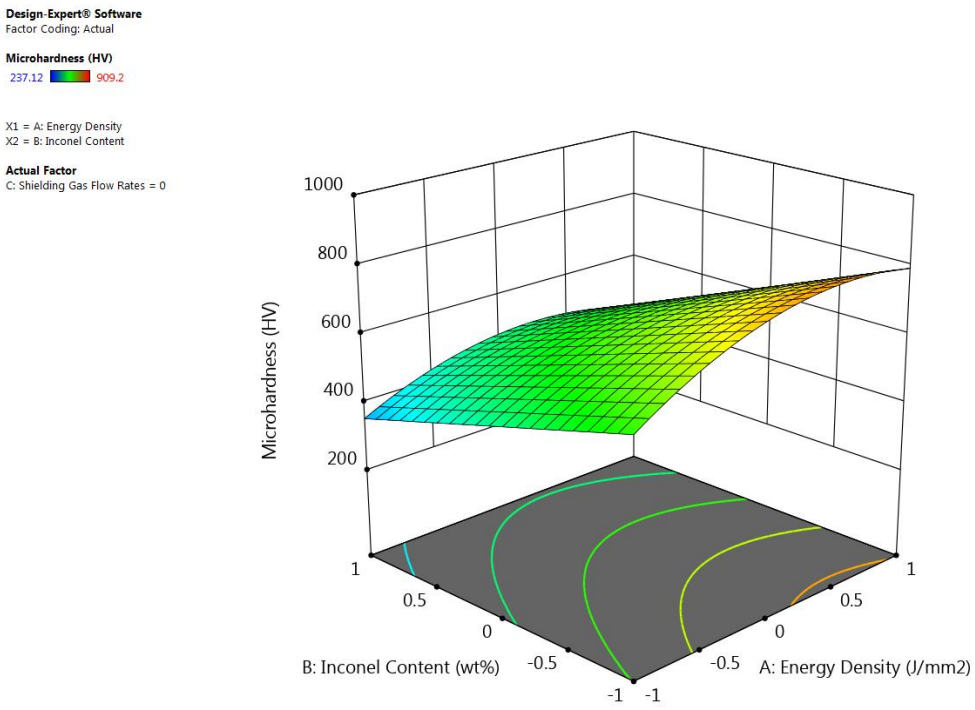

Figure 11: 3-D plots showing the effects of (a) Energy density versus Inconel content, on the microhardness (MH) of the composite coating.

According to Figure 7, the composite's microstructural features which influence its wear attribute and mechanism include (i) the nature of inter-facial bonding between the reinforcing particle and the matrix; (ii) the size and distribution of the retained WC particles within the matrix; (iii) the mean free path between the retained reinforcing particles; (iv) presence or absence of microstructural cracks and porosity; (v) sizes of cracks and porosity; in addition (vi) the distance between cracks and porosity.

Figure 13 elucidates the nature of wear mechanisms encountered by the composite coating as LC process and materials parameters are altered. A study of Figure 13 reveals that the reinforcing particles are deformed into convex shape as the inconel 625 matrix is worn as wear progresses. Considering that WC-86 particles are difficult to be worn out because of their high microhardness, the wear scar of the coatings (Figure 13) consists of plowing, valleys and peaks, and plastic deformation which are characteristics of abrasive wear due to hard body contact [24] while spalling and tearing-off result from the adhesive wear. Furthermore, the convex shape of the reinforcing particles tends to alter the direction of movement of the abrasive, hence, protecting the coating against wear. It is pertinent to note that the reinforcing particles are eventually worn after repeated contact with the counter body such that they break off and become abrasive particles. As a result, the two-body abrasive wear between the composite coating and the counter body consequent become three body abrasive wear (Figures 13a to e). As the reinforcing particles are worn, the matrix and the counter body exhibit adhesive wear. Hence, adhesive, and abrasive wear occurred alternately in the coatings. Severe wear conditions (e.g., as local welding/adhesion and shallow and narrow furrow) are also seen in Figures 13a to e, a confirmation that the wear pattern across the coatings was altered with more mild abrasive wear dominating as both laser energy density and gas flow rates increase while Inconel 625 content reduces in composite coatings. In subsequent paragraphs, the inter-relationship between Figures 7, 12 and 13 are presented to understand how LC process and materials parameters influence the composite coating's wear response.

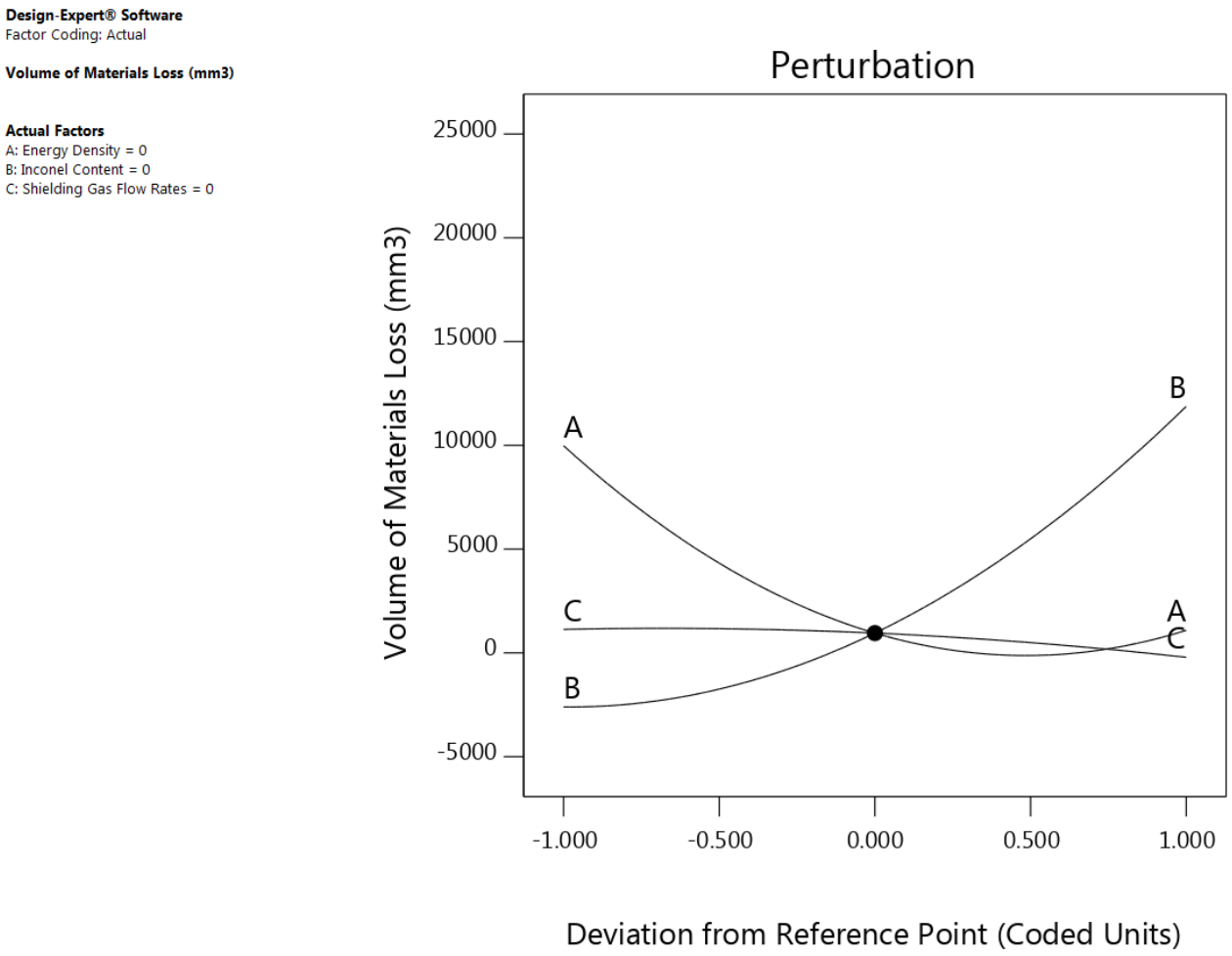

Figure 12: Effects of all factors on the volume of material loss (VML) of the composite coatings

A comparison of Figures 7a and b reveals the following: (i) the sample fabricated with low energy density of 13.1 J/mm^2 (Figure 7a) consists of retained WC particles which are non-uniform in size and distribution within the inconel 625 matrix relative to that fabricated with higher energy density of 21.9 J/mm^2 (Figure 7b); (ii) the average sizes of retained WC-86 particles in Figure 7a are quite bigger than that of Figure 7b; and (iii) the retained WC-86 particles in Figure 7a are not effectively imbedded within the Inconel matrix relative to that of Figure 7b; an indication that the inter-facial bond between the retained reinforcing particles and the Inconel matrix is weaker in Figure 7a in comparison to Figure 7b; (iv) the mean free path between the retained reinforcement particles in Figure 7a is shorter and non-uniform in length in comparison to that of Figure 7b and (v) the presence of cracks and porosity in Figure 7a while no cracks and porosity are present in Figure 7b. Hence, defective microstructure characterised with pores and cracks, the non-uniform distribution, and sizes of the reinforcing particles within the matrix, non-uniform free mean path and mainly unembedded large-sized retained particles within the Inconel matrix point to the fact that lower laser energy density of 13.1 J/mm^2 is incapable consolidating a fully dense composite coating. Meanwhile, increasing the laser energy density to 21.9 J/mm^2 resulted in defect free microstructure, reduced free mean path of the reinforced particles, increased even distribution of the reinforced particles, and small-sized reinforced particles (Figure 7b) which eventually led to reduced VML (improved wear resistance) as seen in Figure 12.

(a) 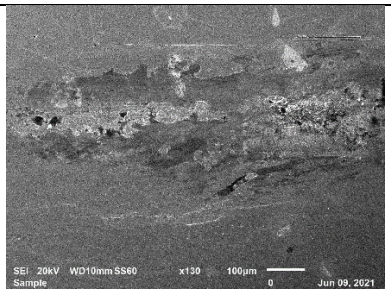
SEI 20kV WD10mm SS60 x130 100µm
Sample 0 Jun 09, 2021

(f) 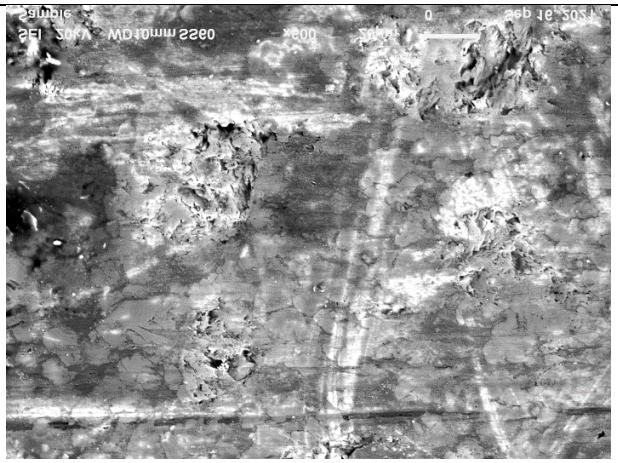

(b) 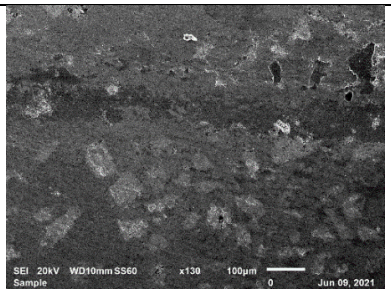
SEI 20kV WD10mm SS60 x130 100µm
Sample 0 Jun 09, 2021

(g) 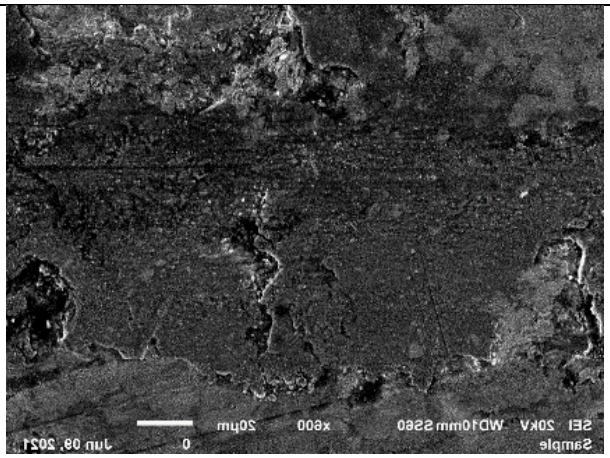

(c) 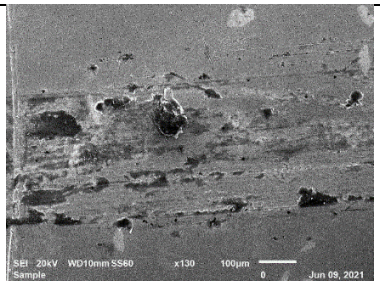
SEI 20kV WD10mm SS60 x130 100µm
Sample 0 Jun 09, 2021

(h) 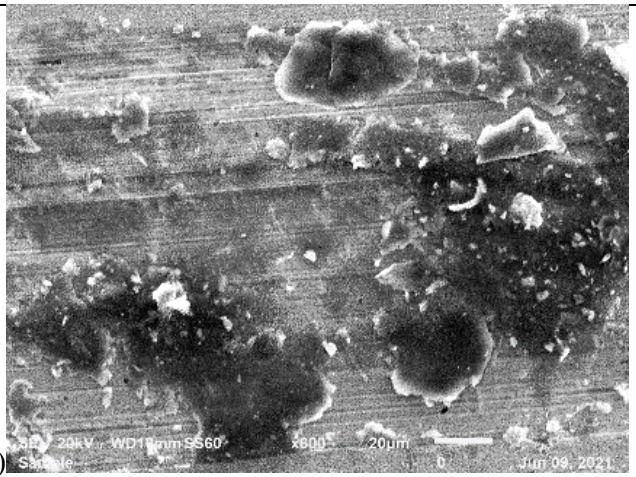
SEI 20kV WD10mm SS60 x800 20µm
Sample 0 Jun 09, 2021

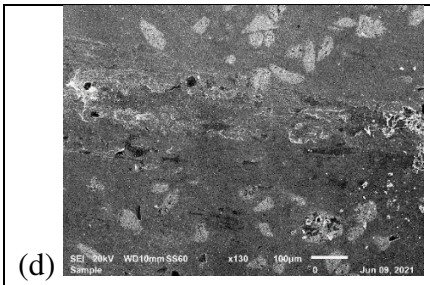

(d)

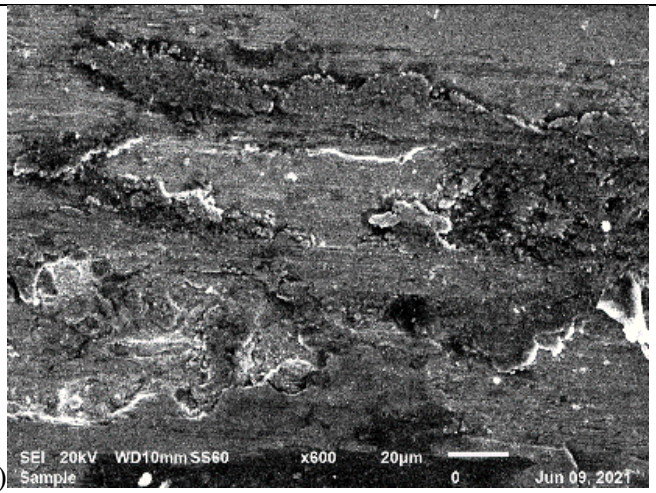

(i)

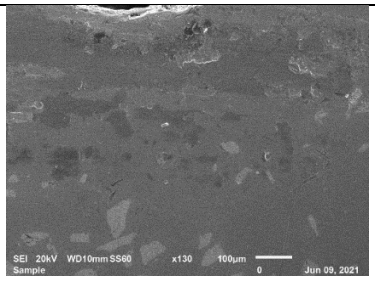

(e)

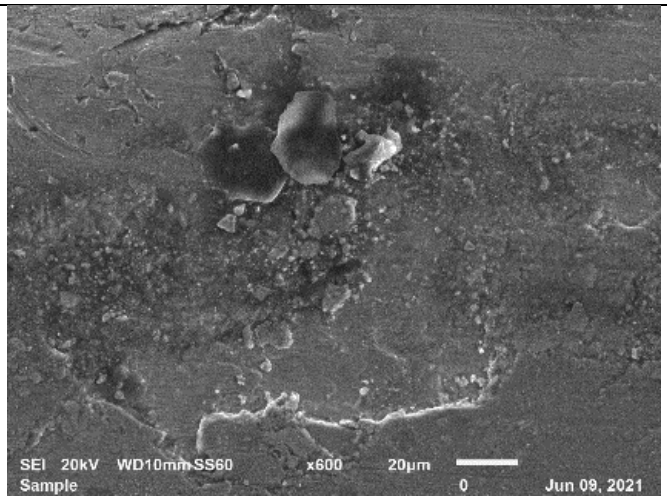

(j)

Figure 13: Scanning electron micrographs showing how wear mechanism of composite coating is influenced by alteration in energy density (a, f) 13.1 J/mm^2, 70wt% In, 12l/min; (b, g) 21.9 J/mm^2 70wt% In, 12l/min; (c, h) 21.9 J/mm^2, 90wt% In, 12l/min; (d, i) 13.1 J/mm^2, 90wt% In, 4l/min; (e, j) 13.1 J/mm^2, 90wt% In, 12l/min.

Figure 13a reveals the occurrence of abrasive wear mechanism which is characterised with deeper furrow, larger wear debris and micro pits. Occurrence of abrasive wear in the sample fabricated with 13.1 J/mm^2 is due to microstructural defects (pores) and large sized WC-86 particles identified in Figure 7a. The pores characterised with sharp edges and excessive local stresses resulted in existence of cracks which contributed to the splitting of the matrix material (inconel 625) as well as it's peeling off into wear debris.

Consequently, abrasive wear was eventually aggravated with the large wear debris penetrating the friction interface, thereby causing secondary wear, and then forming deep furrows and micro pits on the worn surface [24]. Furthermore, the weak interfacial bonding strength between the inconel 625 matrix and the reinforcing WC-86 particles resulting from non-dissolution of the reinforcements because of low laser energy density (13.1 J/mm^2) consequently deteriorated the wear resistance of the composite coating. According to Liu and Shi [24], the presence of undissolved and unbonded large-sized reinforcing particles characterised with sharp edges and corners within the matrix further degenerated the wear resistance of the composite coatings.

The worn surface of the composite coating sample (Figure 13b) fabricated with 21.9 J/mm^2 is characterised with shallow furrow, fine wear debris and plastic deformation, an indication of the occurrence of both abrasive and adhesive wear. This is attributed to the improvement of the toughness of the coating because of the reduction of the hard carbides as well as grain refinement which consequently inhibit material loss due to brittle fracture [25]. Findings from Figures 7a & b and 13a & b align with the outcome from the study by Leech *et al.,* [7] who pointed out that reduced free mean path between the retained large-sized and uniformly distributed reinforcements inhibits the penetration of the abrasives into the ductile inconel 625 matrix, thereby, exhibiting improved wear resistance.

The claim in Figure 12 that VML increases as inconel content increases is corroborated by Figure 7b and c due to (i) the free mean path between the retained reinforced particles increasing, (ii) the size of the reinforced particles reducing and (iii) the uniformity of the distribution of the retained reinforced particles within the inconel matrix deteriorating as inconel content increases. This outcome is accounted for by the fact that reducing content of harder reinforcing WC-86 particles imparted increased free mean path between small-sized retained reinforcements in the composite coating's microstructure degraded the prevalent ductile matrix material, hence, poor wear resistance of the composite coating as inconel content increases. Analysis of the wear mechanisms in Figures 13b and c lend credence to the findings on the effects of inconel content on the wear resistance of the composite coatings. In Figures 13b and c, the friction between the composite coating and the counter body did not occur at the entire surface contact but at points where the protrusion of the composite coating is in contact with the counter body. The local stress at the contact point is quite high because the actual area of contact is very small. Adhesive wear, evident by flaking, occurred in Figures 13b and c through excessive local stress which caused the contact points to weld and then sheared during relative tangential movement which resulted in the peeling off the material [28, 29]. Comparative analysis of Figures 13b and c suggests that reduction in inconel 625 content resulted in smaller spalling area (Figure 13b) relative to higher inconel 625 contents (Figure 13c), an indication that higher content of WC-86 in the composite coating imparts better wear resistance.

A study of Figures 7d and e as well as Figure 12 shows that VML reduces slightly as shielding gas flow rate was increased from 4l/min to 12l/min due to (i) the free mean path between the retained reinforced particles reducing marginally, (ii) the size of the reinforced particles increasing marginally and (iii) the uniformity of the distribution of the retained reinforced particles within the inconel matrix improving marginally. Figures 13d and e support the outcomes on how shielding gas flow rates influence the wear resistance of the composite coatings. The wear mechanism in Figures 13d and e is the same as reported for Figures 13b and c. It can then be concluded that increment in shielding gas flow rates resulted in smaller spalling area (Figure 13e) relative to smaller shielding gas flow rates (Figure 13d), an indication that higher shielding gas flow rates improves wear resistance marginally.

It is evident from Figure 14a that the least desirable wear resistance attribute is obtainable by combining the lowest level of energy density with highest level of inconel content. Wear resistance of the composite coating worsens due to reduced content of hard retained reinforcing particles within the matrix. This outcome could also be attributed to reduced energy density which might have engineered weak inter-facial bonding between the inconel 625 matrix and the reinforcing particles.

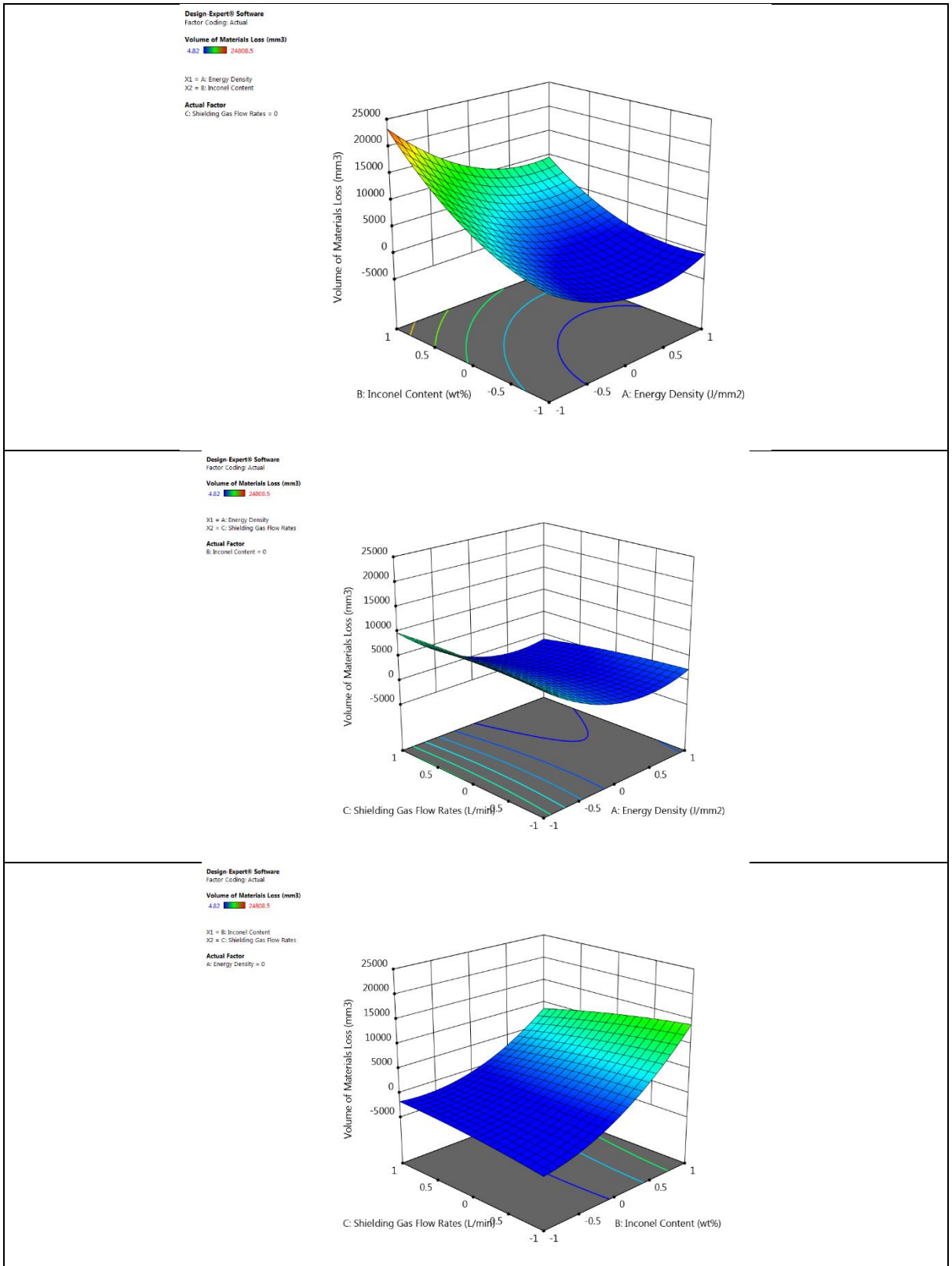

Figure 14: 3-D plots showing the effects of (a) Energy density versus Inconel content, (b) Energy density versus Gas flow rates and (c) Inconel content versus Gas flow rates on the volume of material loss (VML) of the composite coating.

The most desirable wear resistance attribute was attained by combining the laser energy density set at 19.70J/mm^2 with the lowest content of inconel 625 matrix (70wt%). This is accounted for by introducing appropriate laser energy density into the molten pool which imparted stronger inter-facial bonding between the inconel 625 matrix and the reinforcing particles as well as increased content of uniformly distributed retained hard reinforcing particles within the matrix characterised with reduced mean free path between retained particles. Figure 14b reveals that the most desirable wear resistance property is obtainable by combining shielding gas flow rates at any level (4 to 12 l/min) with energy density set at 19.7J/mm^2. This could be explained by the fact that all levels of the shielding gas flow rates impart cooling rates into the molten pool which is sufficient to engineer uniform re-arrangement of the retained reinforcing particles within the ductile inconel 625 matrix coupled with appropriate sizing of retained particles and free mean path between the retained particles. On the contrary, the least desirable wear resistance is imparted into the composite coating by combining lowest level of energy density (13.1J/mm^2) with highest level of shielding gas flow rates (12l/min). Figure 14c reveals that the most desirable wear resistance of composite coatings can be obtained by setting inconel content at 80wt% irrespective of the shielding gas flow rates introduced into the melt pool. On the contrary, setting the inconel content at the highest level (90wt%) combined with shielding gas at the lowest level (4l/min) deteriorates most the wear resistance of the coating. This could be attributed to minimal content of the retained reinforced particles coupled with reduced size of the retained particles and large free mean path between the particles as a result reduced cooling rates of the molten which ensure the small quantity of reinforcing particles available dissolve excessively within the molten pool. Finally, comparative analysis of the influence of the interactions between the factors suggests that energy density/inconel content (27,500mm^3) $>$ inconel content/shielding gas flow rates (19,500mm^3) $>$ energy density/shielding gas flow rates (12,500mm^3). This finding conforms to the F-vales of the interactions of these factors shown in Table 5.

4.4 Optimisation and confirmation: Analysis of interaction between output variables

The need to establish the nature of relationship between CDR, MH and VML is critical designing a composite coating with optimized wear performance at appropriate carbide dissolution ratio. For instance, it is desirable to have a composite coating characterised with high microhardness so that it can resist scratch effectively. Furthermore, the microhardness property exhibited by a composite coating is also a function of the size of the retained reinforcing particle, the mean free path between the retained particles within the ductile matrix and the degree of the uniformity of the distribution of retained particles within the ductile matrix. The nature of the interactions between the laser beam, the shielding gas and the constituents of the composite coatings also play a critical role in the dissolution of carbide from the reinforcing particles which eventually determines the nature of intermetallic phases formed in the composite. High wear resistant composite coating to be fabricated is expected to be characterised with appropriate size of the retained reinforcing particle, appropriate mean free path between the retained particles within the ductile matrix and optimal degree of the uniformity of the distribution of retained particles within the ductile matrix together with the appropriate carbide dissolution ratio (CDR) which leads to formation of intermetallic phases that increases wear resistance of the composite coatings. Analysis of findings from this study suggests that the selection of optimum parameters for improving wear resistance (high MH and low VML) must be carefully selected to ensure appropriate carbide dissolution which imparts appropriate size of the retained reinforcing particle, mean free path between the retained particles within the ductile matrix and optimal degree of the uniformity of the distribution of retained particles into the composite microstructure. Increasing the microhardness and

lowering VML of the coatings demands that less of Inconel 625 needs be blended with increasing content of WC-86, while a medium value of laser energy density is chosen for fabricating the claddings to ensure effective interfacial bonding between the matrix and the reinforcing particle as well as uniform distribution of the reinforcing particles within the ductile matrix at low free mean path between the particles (Figures 9, 11 and 14). As a result, these criteria were employed in guiding the selection of optimum process parameters. Equation x (the desirability function) allows for simultaneous estimation of multiple responses during optimisation [26].

$$\left[\prod_{i=1}^{N} d_i^{r_i}\right]^{1/\sum ri} \quad \text{(x)}$$

N = Number of responses
r_i = The importance of some particular response
d_i = The partial desirability function for specific responses

Desirability function was determined by assigning desirable high or low limit specifications to each response. Optimum process parameters were determined via a range of experimental conditions (Table 1) adopted in this study to identify optimum values of coatings' CDR (75%), MH ($\geq 700\ HV$) while minimising VML ($< 500\ mm^3$). The rationale for this optimisation is premised on the need to produce wear resistant coating. The most desirable experimental conditions are presented in Table 8 and were determined via Design Expert statistical software. As elucidated in Olakanmi *et al* [1], the costs of purchasing (i) shielding gas $<$ (ii) Inconel 625 $<$ (iii) laser energy density were considered when selecting appropriate operating conditions for producing most desirable wear resistant composite coatings. Therefore, it is desired that optimum composite coatings are produced with minimum laser energy density which cost least in comparison to the cost of Inconel 625 and shielding gas.

Table 8: Parametric and response constraints for optimising the composite coatings

Name	Goal	Lower Limit	Upper Limit	Lower Weight	Upper Weight	Importance
A:Energy Density	is in range	-1	1	1	1	3
B:Inconel Content	is in range	-1	1	1	1	3
C:Shielding Gas Flow Rates	is in range	-1	1	1	1	3
Carbide Dissolution Ratio	is target = 75	50	90	1	1	3
Microhardness	is target = 700	237.12	909.2	1	1	4
Volume of Materials Loss	minimize	4.82	24808.5	1	1	4

Table 9 shows that the optimum experimental conditions are energy density = 19.67J/mm^2; inconel content = 70wt%; and shielding gas flow rates = 6.0 l/min. This optimum operating

condition has a desirability value of 1.00 with optimising coatings' CDR = 75%, MH > $700\ HV$; and VML ($< 500\ mm^3$). Findings from the confirmatory experiment indicate that composite coatings with the desired wear resistance specifications can be fabricated via the identified optimal process parameters. Experimental outcomes are in good agreement with predicted results with the error ranging between +2 to 6% (Table 9) with the exception of VM (see earlier discussion in section 3.2). Figure 15 shows that the optimum coating is free of defects and characterised with coherently bonded substrate-coating inter-face (Figure 15a) and fully consolidated microstructure with uniformly distributed WC-86 particles within the Inconel 625 matrix (Figure 15b). For the optimum sample, the mean free path between the retained reinforced particles and the size of the reinforced are estimated to be 40 μm and 30μm respectively (Figure 15b). These microstructural parameters contributed to improved wear resistance reported for the optimum samples as evident by very low VML = 9.42 mm^3 when CDR was 77.08% and MH = 852.59 HV at the selected LC process and materials parameters.

Table 9: Optimal confirmatory tests comparing the experimental and predicted outcomes

Energy density (ED)	**Inconel content (In)**	**Gas flow (G)**		**CDR**	**MH**	V_f
19.7	70.0	6.0	Measured	77.08	852.59	9.42
(0.5)	(-1)	(0.5)	Predicted	74.93	809.52	-2242.89
			Error (%)	2.87	5.40	-1004.20

4. CONCLUSIONS

A new insight on the nature of relationships between laser processing and material parameters on one hand and Inconel 625 wear performance and carbide dissolution ratio (CDR) on the other hand has been gained from this study. The inter-relationship between the microstructural characteristics, CDR and wear performance of the coatings is established to design a most desirable wear resistant composite coating. Findings from this study are as follows:

➢ Laser energy density and inconel 625 content significantly influenced MH and VML whereas only energy density significantly in-fluences CDR of the fiber-laser deposited Inconel 625/WC-86 composite coatings.

➢ CDR increases with laser energy density. MH increases with laser energy density up to a threshold of 19.70J/mm^2 (0.5 coded unit). Further increase in energy density above the threshold value results in reduction in MH of the coatings. Increase in laser energy density above 19.70J/mm^2 reduces the wear resistance of the coating with VML increasing.

➢Inconel 625 content varies directly with CDR and VML while it has an indirect relationship with MH.

➢The shielding gas flow rates have no effect on micro-hardness whereas it varies indirectly with CDR and VML.

(a)

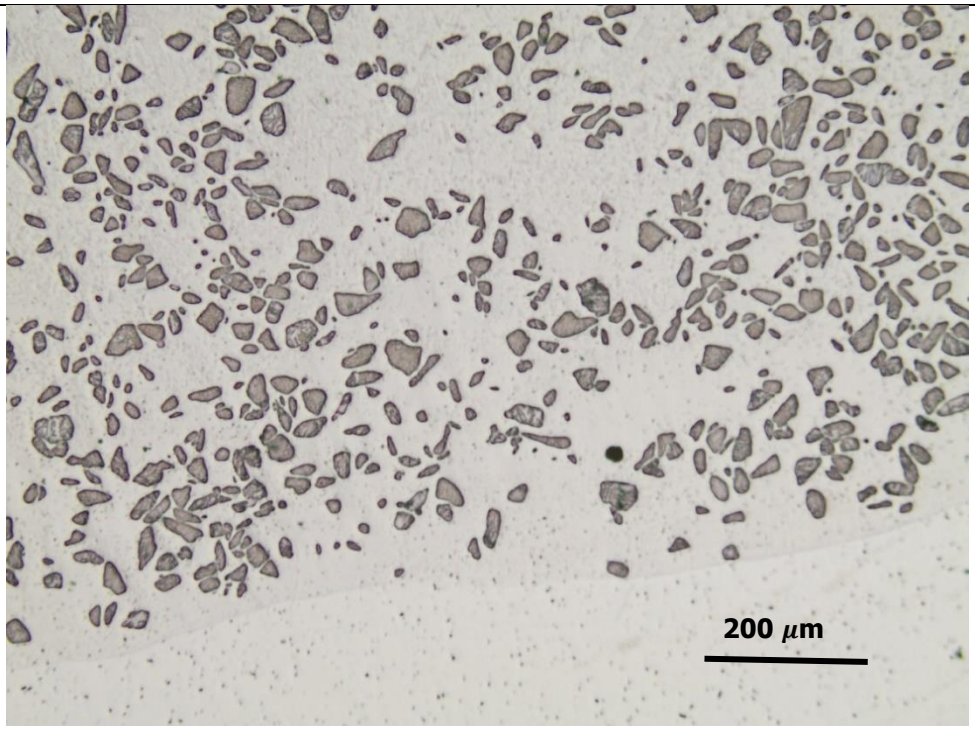

(b)

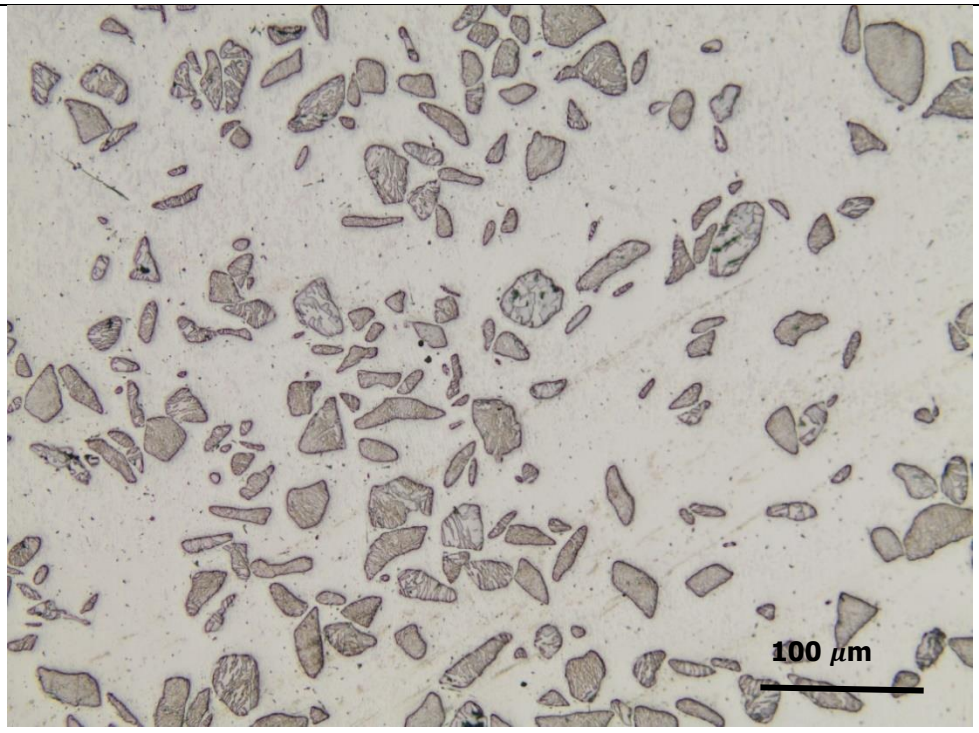

Figure 15: Micrograph of defect-free optimum coating showing (a) coherently bonded substrate-coating inter-face and (b) fully consolidated microstructure with uniformly distributed WC-86 particles within the Inconel 625

- Optimum processing conditions obtained via desirability value of 1.00 yielded are energy density = 19.70 J/mm^2; inconel content = 70wt%; and shielding gas flow rates = 6.0l/min. Experimental responses of the coatings obtained via the optimum

processing parameters are CDR = 77.08%, MH = 852.59 $HV_{0.3}$ and VML = 9.42mm^3 within the error of 6%.

- For optimum sample, the mean free path between the retained reinforced particles and the size of the reinforced are estimated to be 40 μm and 30μm respectively. These microstructural parameters contributed to improved wear resistance reported for the optimum samples as evident by very low VML = 9.42 mm^3 when CDR was 77.08% and MH = 852.59 HV at the selected LC process and materials parameters.

- It may be inferred that the developed RSM mathematical models are reliable and adequate in predicting the CDR and wear resistance attributes of the fiber-laser deposited composite coatings. Finally, the inter-relationship between the CDR and wear performance are established towards designing a composite coating with optimized wear resistance at appropriate carbide dissolution ratio.

Funding:
This research is supported by the African Laser Center (ALC) under Grant no. CSIR-NLC Reference LHIL 500 task ALC R008 & R010 and Botswana International University of Science & Technology (BIUST)Research Initiation Fund under Grant no. BIUST/ds/r&I/7/2016.

Acknowledgement:

The authors are grateful to Mr. Samuel Skhosane for his assistance in operating the laser facility at CSIR.

Conflicts of interest: The authors declare that they have no conflict of interest.

Declaration:

The authors declare that they have no conflict of interest. Every author listed in this manuscript agreed to participate in this research and confirms that the manuscript has never been published in any other journal. In addition, all authors have approved the contents of the manuscript and have agreed to the International Journal of Advanced Manufacturing Technology (IJAMT) publication policies. Based on our knowledge, we have no conflict in anyhow with the above suggested reviewers. We have no dispute however in any sort of interest or financial terms.

Author's Contributions

Conceptualization: EOO, investigation; EOO, SH, SLP, methodology, EOO, SH, SLP, SAL, resources; SLP, SH and EOO, writing of original draft; EOO, writing of review and editing; EOO SH, SLP and SAL funding acquisition. EOO and SLP All authors have read and agreed to the published version of the manuscript.

5. REFERENCES

[1] Olakanmi EO, Nyadongo ST, Malikongwa K, Lawal S. A, Botes A, Pityana SL (2019) Multi-variable optimisation of the quality characteristics of fiber-laser cladded Inconel-625 composite coatings. Surf Coat Technol 357:289–303. DOI: 10.1016/j.surfcoat.2018.09.063

[2] Tobar MJ, lvarez CA´, Amado JM, Rodrı´guez G, Ya´n˜ez A (2006) Morphology and characterization of laser clad composite NiCrBSi–WC coatings on stainless steel. Surf Coat Technol 200: 6313–6317.

[3] Abioye TE, Folkes J, Clare AT, McCartney D (2013) Concurrent Inconel 625 wire and WC powder laser cladding: process stability and microstructural characterisation. J Surf Eng 29: 647–653.

[4] Wang Y, Guo H-B, Peng L-Q, Gong S-K (2011) Processing and microstructure of NiRuAl diffusion barrier coating on Ni-based superalloy. J Surf Eng 27:253–258.

[5] Cooper KP, Slebodnick P, Thomas, ED (1996) Seawater corrosion behavior of laser surface modified Inconel 625 alloy. Mater. Sci. Eng. A A206:138–149.

[6] Huang SW, Samandi M, Brandt M (2004) Abrasive wear performance and microstructure of laser clad WC/Ni layers. Wear 256:1095–1105.

[7] Leech PW, Li XS, Alam N (2012) Comparison of abrasive wear of a complex high alloy hard-facing deposit and WC–Ni based metal matrix composite. Wear 294–295:380–386.

[8] Yutao L, Kaiming W, Hanguang F, Xingye G, Jian L (2022) Microstructure and wear resistance of in-situ TiC reinforced AlCoCrFeNi-based coatings by laser cladding. App Surf Sci 585:152703

[9] Li W, Yang X, Xiao J, Hou Q (2021) Effect of WC mass fraction on the microstructure and friction properties of WC/Ni60 laser cladding layer of brake discs. Ceram Inter 47(20):28754-28763.

[10] van Acker K, Vanhoyweghen D, Persoons R, Vangrunderbeek J (2005) Influence of tungsten carbide particle size and distribution on the wear resistance of laser clad WC/Ni coatings. Wear 258(1–4):194–202.

[11] Zhou R, Jiang Y, Lu D (2003) The effect of volume fraction of WC particles on erosion resistance of WC reinforced iron matrix surface composites., Wear, 255(1–6):134–138.

[12] Zhou S, Huang Y, Zeng X, Hu Q (2008) Microstructure characteristics of Ni-based WC composite coatings by laser induction hybrid rapid cladding. Mater. Sci. Eng. A, A480(1–2):564–572.

[13] Abioye TE, Farayibi PK, McCartney DG, Clare AT (2016) Effect of carbide dissolution on the corrosion performance of tungsten carbide reinforced Inconel 625 wire laser coating. J Mater Proc Technol 231:89-99

[14] Olakanmi EO, Tlotleng M, Meacock C, Pityana SL, Doyoyo M (2013) Deposition Mechanism and Microstructure of Laser Assisted Cold Sprayed (LACS) Al12wt%Si Coatings: Effects of Laser Power. J Mater (JOM) 65(6):776-783.

[15] Olakanmi EO. (2015) Optimisation of the quality characteristics of laser assisted cold sprayed pure aluminium coatings using Taguchi method of experimental design. Mater Manuf Proc 31(11):1490-1499 (DOI: 10.1080/10426914.2014.984306)

[16] Qu J, Truhan JJ (2006) An efficient method for accurately determining wear volumes of sliders with non-flat wear scar and compound curvatures. Wear 261:848 – 855.

[17] Hofmeister W, Griffith M, Ensz M, Smugeresky J (2001) Solidification in direct metal deposition by LENS processing. J Mater (JOM) 53(9):30–34.

[18] Zeng M, Yan H, You B, Hu Z (2021) Microstructure, microhardness and corrosion resistance of laser cladding Ni−WC coating on AlSi5Cu1Mg alloy. Trans Nonferrous Met. Soc. China 31:2716−2728

[19] Meng G, Zhu L, Zhang J, Yang Z, Xue P (2021) Statistical analysis and multi-objective process optimization of laser cladding TiC-Inconel718 composite coating. Optik 240:166828

[20] Abioye TE (2014) Laser Deposition of Inconel 625/Tungsten Carbide Composite Coatings by Powder and Wire Feedstock. Dissertation, The University of Nottingham

[21] Al-Hamdani KS, Murray JW, Hussain T, Clare AT (2019) Controlling ceramic-reinforcement distribution in laser cladding of MMCs. Surf. Coat Technol. 381:125128, doi: 10.1016/j.surfcoat.2019.125128.

[22] Xu P, Zhu L, Xue P, Yang Z, Wang S, Ning J et al (2022) Microstructure and properties of IN718/WC-12Co composite coating by laser cladding. Ceram Inter, 48(6):7905 -7917

[23] Chaudhari PD, More NN (2014) Effects of welding process parameters on microhardness and microstructure. Int. J. Eng. Res. Technol. 3(5):1937–1942.

[24] Liu J, Shi Y (2021) Microstructure and wear behavior of laser-cladded Ni-based coatings decorated by graphite particles. Surf Coat Technol, 412:127044.

[25] Wang W, Lian JB, Ru HQ (2012) Pressureless sintered SiC matrix toughened by in-situ synthesized TiB_2: process conditions and fracture toughness. Ceram. Int. 38:2079–2085, https://doi.org/10.1016/j.ceramint.2011.10.045.

[26] Wei M, Yu H, Song Z, Yin Y, Zhou X, Wang H, et al (2021) Microstructural evolution, mechanical properties and wear behavior of in-situ TiC-reinforced Ti matrix composite coating by induction cladding. Surf Coat Technol, 412:127048.

[27] Sun Y, Hao M (2012) Statistical analysis and optimization of process parameters in Ti6Al4V laser cladding using Nd:YAG laser. Opt. Lasers Eng. 50(7):985–995.

[28] Lei JB, Shi C, Zhou SF, et al (2018) Enhanced corrosion and wear resistance properties of carbon fiber reinforced Ni-based composite coating by laser cladding. Surf. Coat. Technol. 334:274–285.
[29] Xiao Q, Sun WL, Yang KX, Xing XF, Chen ZH, et al (2021) Wear mechanisms and micro-evaluation on WC particles investigation of WC-Fe composite coatings fabricated by laser cladding. Surf. Coat. Technol. 420:127341